



Microstructure and Tribological Properties of Ni-Based Laser-Clad Coatings by Rare Earth Modification

Huaifeng Zhuang¹ · Qian Zhang² · Dingli Zhang¹

Submitted: 24 October 2020 / in revised form: 2 February 2021 / Accepted: 20 February 2021 / Published online: 23 May 2021
© ASM International 2021

Abstract TiC + TiB₂ + Ti₂Ni-reinforced Ni-based laser-clad coatings were prepared on Ti-6Al-4V by CeO₂ modification. The forming quality, microstructure, element distribution, microhardness and wear resistance of the coatings were studied. The results showed that adding 2 wt.% CeO₂ effectively eliminated cracks but led to the micro-pores. The coatings mainly consisted of TiC, TiB₂, Ti₂Ni and matrix α -Ti. When 2 wt.% CeO₂ was added, the coating microstructure was remarkably refined, uniform and dense, and exposed surface area of matrix decreased. TiC changed from dendritic to petal-shaped and granular, TiB₂ from long rod-shaped to short rod-shaped, Ti₂Ni from irregular bulk-like to microporous irregular bulk-like. Al, Cr, Fe and Si distributed uniformly in the Ni-rich matrix, and V was mainly segregated on the TiB₂. Ce₂O₃ particles formed by the decomposition of CeO₂ in the coating mainly distributed around TiC. The planar lattice disregistry δ between the interface (10 $\bar{1}$ 0) of Ce₂O₃ and the interface (110) of TiC was 4.00%, and Ce₂O₃ could act as the nucleation substrate to effectively refine TiC. With the addition of CeO₂, the microhardness was increased, and the wear depth, wear volume and friction coefficient were decreased. 2CeO₂ coating exhibited the best wear resistance and anti-friction compared with 0CeO₂ coating and exhibited an abrasive wear pattern.

Keywords CeO₂ · laser cladding · microstructure · planar lattice disregistry · Ti-6Al-4V · tribological properties

✉ Huaifeng Zhuang
774742827@qq.com

¹ Sino-European Institute of Aviation Engineering, Civil Aviation University of China, Tianjin 300300, China

² College of Aeronautical Engineering, Civil Aviation University of China, Tianjin 300300, China

Introduction

Ti-6Al-4V belongs to the martensitic $\alpha + \beta$ -type dual-phase titanium alloys, which has been widely used in transportation, aerospace, petrochemical, energy, biomedicine and other industrial fields due to its low density, high specific strength, good toughness and strong corrosion resistance (Ref 1-3). However, the safety and durability of Ti-6Al-4V are greatly limited during service time by the low hardness, weak plastic shear resistance and poor wear resistance (Ref 4-6). Surface modification is an effective means to improve the properties of metallic materials, including nitriding, carburizing, ion implantation, laser cladding, chemical vapor deposition (CVD), high-velocity oxygen fuel spraying (HVOFS), physical vapor deposition (PVD) and plasma spraying, etc. (Ref 7-10). The effect of nitriding, carburizing, ion implantation, CVD and PVD on surface modification of titanium alloy is limited by the thickness of surface modification layer, thus leading enormous challenges to the treatment process (Ref 9-13). HVOFS and plasma-sprayed ceramic coatings often have more micro-defects (Ref 14-16). In comparison, laser cladding possesses the potential advantages of high production efficiency, narrow heat-affected zone, high bonding strength between cladding layer and substrate, and compact microstructure, which is extensively applied into the field of repairing titanium alloy components (Ref 17-19).

Laser-clad MMC coatings are most often of the type NiBSi with tungsten carbide as the hard phase, which have been widely used to improve the wear resistance of titanium alloy. To date, Ni-based laser cladding layer on titanium alloy has attracted much interest attributing to its high hardness and tribological properties. Generally, the self-fluxing alloy powders containing B, C and Ni (such as

Ni₂₅, Ni₄₅, Ni₆₀, NiCr-Cr₃C₂, NiCrBSi, NiCrBSiC) are selected as the cladding materials to in situ synthesize Ti-B, Ti-C, Ti-Ni hard phases-reinforced Ni-based coatings (Ref 17, 18, 20–22). For example, Sun et al. (Ref 23) prepared a TiB₂ + TiC particles-reinforced Ni-based composite coating by laser cladding on Ti-6Al-4V alloy with NiCrBSiC powders, and they found that the coating microstructure was uniform, the microhardness increased approximately three times as compared with Ti-6Al-4V alloy, the wear mass loss was considerably lower than that of the Ti-6Al-4V alloy, exhibiting excellent wear resistance. Yan et al. (Ref 22) selected Ti-Si-C system and NiCrBSi powder as raw materials to synthesize a Ti₃SiC₂ + Ti₅Si₃ + TiC-reinforced Ni-based self-lubricating laser-clad coating on Ti-6Al-4V surface. Their results demonstrated that the hardness and tribology of the coating were remarkably enhanced compared with that of Ti-6Al-4V thanks to the reinforcing phases. Similarly, Li et al. (Ref 24) found that NiCrBSi cladding materials could endow Ni-based wear-resistant laser cladding layer with outstanding mechanical properties. Wu et al. (Ref 25) fabricated a Ti(C, N) particles-reinforced Ni-based composite coating by laser cladding on Ti-6Al-4V alloy with 88 wt.% Ni₆₀ + 2 wt.% C + 10 wt.% TiN mixed precursor materials. The microhardness of the composite coating was improved by a factor of 1.8 as against the substrate, and the wear volume loss was reduced by 11.2 times compared with Ti-6Al-4V, which proved that the coating presented a better abrasion resistance.

However, due to the incompatibility between cladding material and substrate, the Ni-based coating is prone to crack initiation, which significantly hinders the popularization and application of the coating (Ref 26, 27). At present, crack susceptibility of the coating is often reduced by preheating the substrate, optimizing process parameters and adding compatible alloy powder or rare earth (Ref 28–30). Among them, adding compatible alloy powder is considered as an effective and simple method to inhibit and eliminate the coating cracks (Ref 31). Some studies proved that adding sufficient Ti-6Al-4V powders into the cladding material could augment the compatibility between the coating and Ti-6Al-4V substrate, thus improving the forming quality of the coating (Ref 32–34). However, the excessive addition of Ti-6Al-4V powder will lead to a strong decrease in the coating hardness, which is not suitable for working under harsh wear conditions. Therefore, it is of great significance to ensure that the coating exhibits higher hardness and perfect forming quality simultaneously. Recently, numerous studies have shown that CeO₂ can refine the microstructure, eliminate the cracks, ameliorate the uniformity of the microstructure, inhibit the microstructure segregation, augment the plastic toughness of the cladding layer and enhance the plastic deformation

resistance (Ref 35–37). Ding et al. (Ref 38) investigated the effect of CeO₂ on Co-based composite coatings on the surface of SPHC steel by laser cladding technology and concluded that the 1.5 wt.% CeO₂ coating had excellent appearance quality and satisfactory wear resistance. Wang et al. (Ref 39) produced a Ni-based composite coating on AISI 1045 steel, and they found that CeO₂ promoted the convection of molten pool, refined the microstructure, lowered the inclusion content and accelerated the densification of microstructure. Hence, the microhardness and tribological properties were greatly ameliorated. Li et al. (Ref 40) synthesized a Ti₃Al/γ-Ni-based laser cladding layer on Ti-6Al-4V with Ti₃Al + Ni/Cr/C + TiB₂/Al₂O₃ + SiC/nano-CeO₂, and the results showed that the addition of 1.5 wt.% nano-CeO₂ could decrease the crack tendency. Furthermore, nano-CeO₂ had a surface effect to suppress the crystallization and growth of the crystals; therefore, the 1.5 wt.% nano-CeO₂ coating exhibited higher hardness as well as better wear resistance compared with the 0 wt.% nano-CeO₂ coating and substrate. Liu et al. (Ref 31) prepared TiC/Ti₂Ni-reinforced Ti-based wear-resistant coatings with Ti-6Al-4V + Ni₆₀ + CeO₂ cladding powders on Ti-8Al-1Mo-1V alloy surface, and they found that appropriate amount of CeO₂ could effectively relieve the residual stress, thus reducing the tendency of crack formation in the coating. Moreover, CeO₂ could significantly refine the microstructure, promote the homogeneity of microstructure and enhance the coating wear resistance. Therefore, CeO₂ provides an approach for improving the forming quality and mechanical properties of the coating.

However, to the best knowledge of authors, the effect of CeO₂ on the forming quality, phase, microstructure, element distribution and tribological properties of Ni-based composite coatings on Ti-6Al-4V is rarely reported. Herein, the TiB₂ + TiC + Ti₂Ni-reinforced Ni-based wear-resistant laser-clad coatings were produced on Ti-6Al-4V by coaxial powder feeding laser cladding with the novel Ti-6Al-4V + Ni₄₅ + NiCr-Cr₃C₂ + CeO₂ mixed powders. The aim of this work was to ameliorate wear resistance of Ti-6Al-4V and investigate the influence of CeO₂ on the forming quality, phase composition, microstructure, microhardness and tribological properties of the coatings. We hope to provide some reference for the research and application of Ni-based composite coating on titanium alloy surface.

Experimental Procedures

Materials

Annealed Ti-6Al-4V alloy with the thickness of 10 mm was selected as the substrate material, whose

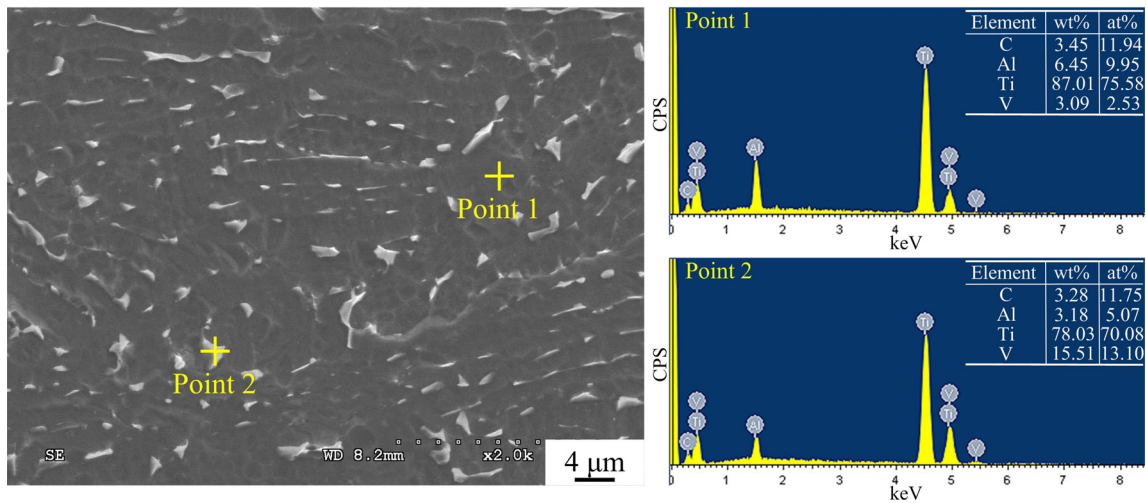


Fig. 1. Microstructure and EDS results of Ti-6Al-4V.

microstructure is shown in Fig. 1. It was clearly seen from Fig. 1 that Ti-6Al-4V comprised of black α -Ti phase (hexagonal close-packed structure, HCP) and bright white β -Ti phase (body-centered cubic structure, BCC) (Ref 41). The EDS results of α -Ti (Point 1) and β -Ti (Point 2) show that Al element was mainly in α -Ti and V in β -Ti, and the reason might be that Al is a stabilizing element for α -Ti and has a high solid solubility in α -Ti phase (Ref 42), and vice versa. The impurities and oxides on the substrate surface were removed by surface sandblasting technology, cleaned with absolute ethanol for 30 min and then placed in a vacuum drying box for use.

The cladding materials selected were Ti-6Al-4V (granulometry of 20–150 μm), Ni45 (granulometry of 40–150 μm), NiCr-Cr₃C₂ (granulometry of 50–150 μm) and CeO₂ (granulometry less than 50 μm) mechanically mixed powders (see Table 1). The SEM morphologies of each spherical powder are shown in Fig. 2. The elemental composition of Ti-6Al-4V, Ni45 and NiCr-Cr₃C₂ is shown in Table 2.

Laser Cladding Experiment

Trudisk 4002 fiber laser was selected for laser cladding experiment, of which the energy output was very stable and the laser power (the maximum reaches 6000 W) was continuously adjustable. The substrate was laser processed by coaxial powder feeding method. The actual processing and schematic diagram are presented in Fig. 3(a) and (b). Helium (He) and argon (Ar) are used as powder feeding gas and shielding gas during laser cladding, respectively. In this study, the coaxial powder feeding laser cladding technology adopted carrier gas (Helium) powder feeding method, which could provide stable powder conveying capacity of cladding materials by controlling the rotation

Table 1 Laser cladding material system ratio (wt%)

No.	Ti-6Al-4V	Ni45	NiCr-Cr ₃ C ₂	CeO ₂
0CeO ₂	20	70	10	0
2CeO ₂	20	68	10	2

rate of powder feeder. In addition, the helium has good fluidity and can effectively avoid the oxidation of cladding materials. During laser cladding, the laser beam, cladding material and shielding gas (Argon) enter from the corresponding channel of the nozzle and shoot out at the end of the nozzle. The laser beam profile conforms to the Gaussian distribution, presenting the characteristics of high energy in the central region and low energy at the edge. The laser beam passes along the central axis of the nozzle and gradually converges. The cladding materials meet with the laser beam at the nozzle under the action of gravity and helium, and rapidly melt on the substrate surface to form a molten pool. As the shielding gas, the density of argon is close to the air and the fluidity of argon is poor, which is easier to cover on the surface of molten pool to prevent the oxidation of the laser-clad coatings. The optimized process parameters are shown in Table 3.

The penetrant testing (PT) technique was used for detecting the coating cracks. The cross-sectional morphology was characterized with the help of optical microscopy (OM, Leica DVM6, Germany). The x-ray diffraction (XRD, SmartLab 9kw, Japan) was used to analyze the precipitated phases in the composite coatings, with the specific parameters: Cu target and K α radiation with a wavelength of 0.15406 nm, voltage of 40 kV, current of 150 mA, scanning velocity of 6°/min, scanning range of 10°–60°, 2 θ scanning step of 0.02°, time step of 0.15 s. The

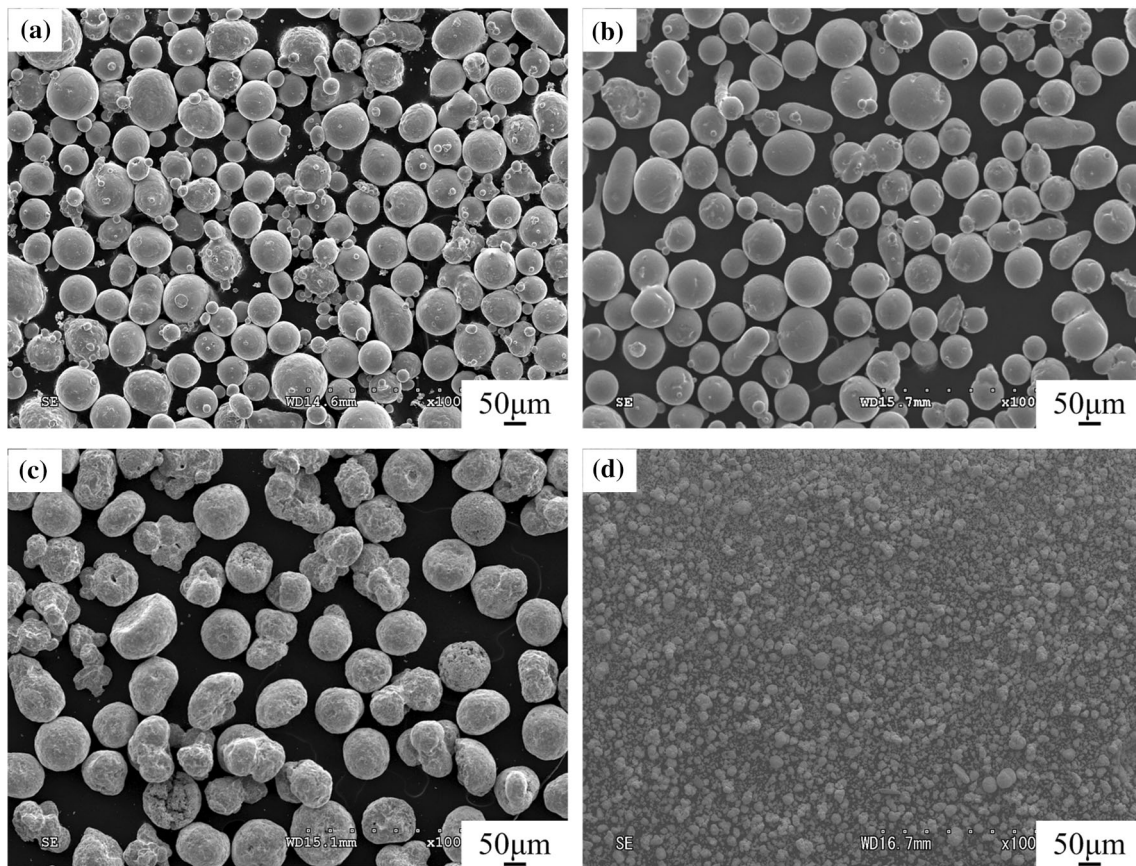


Fig. 2. Morphologies of each powder: (a) Ti-6Al-4V; (b) Ni45; (c) NiCr-Cr₃C₂; (d) CeO₂.

Table 2 Elemental composition of Ti-6Al-4V, Ni45 and NiCr-Cr₃C₂ (wt%).

Materials	B	C	N	O	Si	Al	V	Cr	Fe	Ni	Ti
Ti-6Al-4V	...	0.10	0.05	0.20	...	5.5-6.8	3.5-4.5	...	0.30	...	Bal.
Ni45	3.5-5.5	0.3-0.6	4.5-6.5	10-14	≤ 5	Bal.	...
NiCr-Cr ₃ C ₂	...	9.2-10.7	Bal.	...	18-22	...

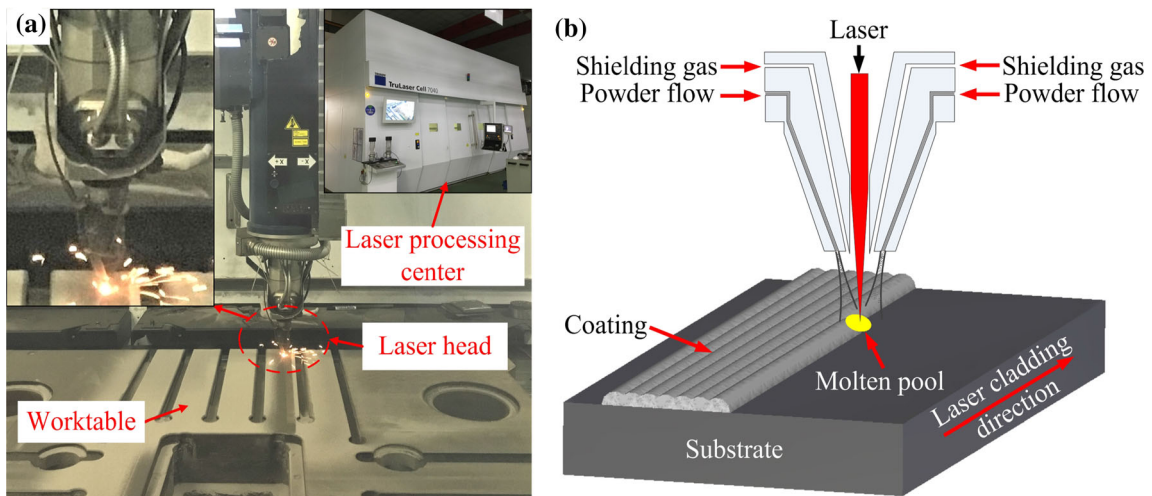
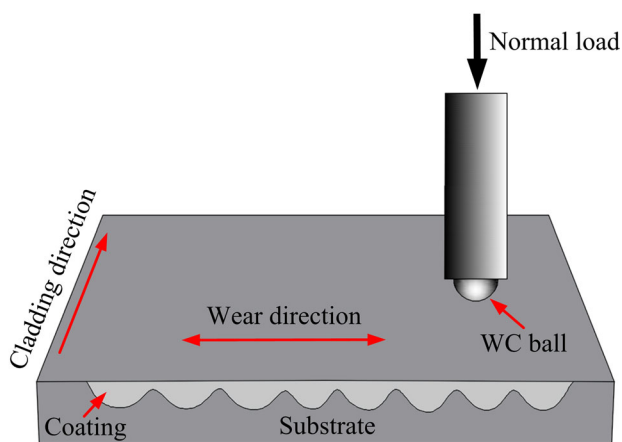


Fig. 3. (a) Actual processing; (b) schematic diagram.

Table 3 Process parameters.

Parameters	Value	Unit
Power	900	W
Scanning speed	400	mm/min
Laser wavelength	1030	nm
Spot diameter	3.0	mm
Rotation rate of powder feeder	1.2	r/min
Gas flow rate of helium	7.0	L/min
Gas flow rate of argon	11.0	L/min
Focal length	16	mm
Overlap ratio	0.5	1

**Fig. 4.** Schematic diagram of reciprocating tribological properties test process.

scanning electron microscopy (SEM, Hitachi S-3000N, Japan) was used to observe the coating microstructure. The energy-dispersive spectrometry (EDS, Oxford INCA PentaFET-X3, UK) was applied to analyze the element composition of the constituents. The element distribution was characterized by scanning electron microscopy (SEM, Carl Zeiss Sigma 500, Germany) and field emission electron probe x-ray microanalyzer (EPMA, JXA-8530F, Japan). The microhardness was measured with a spacing of 0.1 mm by a microhardness tester (Wilson Tukon 2500, USA) with a normal load of 9.8 N and a dwell time of 12 s. The tribological properties were tested by a tribometer (RTEC MFT-5000, USA) with a normal load of 100 N at 25 °C by a WC ball ($D = 6$ mm), the reciprocating wear sliding velocity was 3.6 m/min, and the total distance was 5.4 m with a sliding time of 90 s. The schematic diagram of reciprocating tribological properties test process is shown in Fig. 4. A white-light interfering profilometer (RTEC UP, USA) was applied to characterize the wear parameters and worn surface morphologies.

Results and Discussion

PT Results, Surface and Cross-Sectional Morphology

Figure 5 shows the PT results, surface and cross-sectional morphology of the coatings. Figure 5(a) and (b) shows the PT results and surface morphology of the coatings. It can be clearly seen from Fig. 5(a) and (b) that the coating macro-surfaces with different CeO_2 content were continuous, uniform and flattened; moreover, no uplift and ablative phenomena were observed. However, the PT results show that there were a large number of oblique cracks on the surface of the 0 CeO_2 coating, which basically penetrated the coating macro-surface and had a certain angle along the cladding direction. The possible reasons for the formation of cracks are as follows: (a) There are certain differences in thermophysical properties between cladding materials and substrate material, and laser cladding is a rapid melting and solidification process; therefore, it is easy to generate a stress concentration due to the thermal expansion and contraction effect, thus causing the crack initiation (Ref 43). (b) During the rapid solidification process, the coarse and developed dendrites or hard reinforcing phases have strong structure collision, which will cause large residual stress at the interface with different growth orientations and form micro-cracks (Ref 44); then, the micro-cracks further expand into macro-surface cracks as shown in Fig. 5(a). From Fig. 5(b), the PT results show that no cracks were found on the 2 CeO_2 coating surface, indicating that the addition of CeO_2 could effectively inhibit the crack initiation. The satisfactory results can be explained as follows. CeO_2 can refine the microstructure, enhance the convection of molten pool, accelerate the homogeneity of coating microstructure and finally reduce the stress concentration phenomenon (Ref 31, 35–37). Therefore, the formation of cracks is restrained or eliminated. Figure 5(c) and (d) illustrates the cross-sectional morphology of 0 CeO_2 and 2 CeO_2 coatings. As seen in Fig. 5(c), the thickness of 0 CeO_2 coating was about 1.20 mm, and there were obvious penetrating cracks, which terminated at the interface between the coating and substrate. The reason might be that martensitic transformation was induced by thermal stress in the heat-affected zone (HAZ), resulting in thermal deformation and volume expansion, which led to the formation of compressive stress and inhibited the further propagation of cracks. Figure 5(d) shows that the thickness of 2 CeO_2 coating is about 1.25 mm, and the cross section of the coating is free of cracks but a few visible micropores. The formation of micropores might be attributed to the following two reasons: (a) A small amount of reactive gas generated in the laser cladding process could not

Fig. 5. Surface qualities and PT results for the coatings: (a) 0CeO₂; (b) 2CeO₂. Cross-sectional morphology of the coatings: (c) 0CeO₂; (d) 2CeO₂.

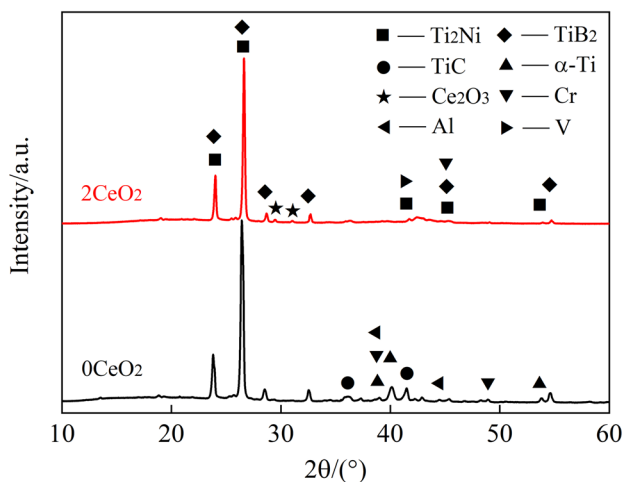
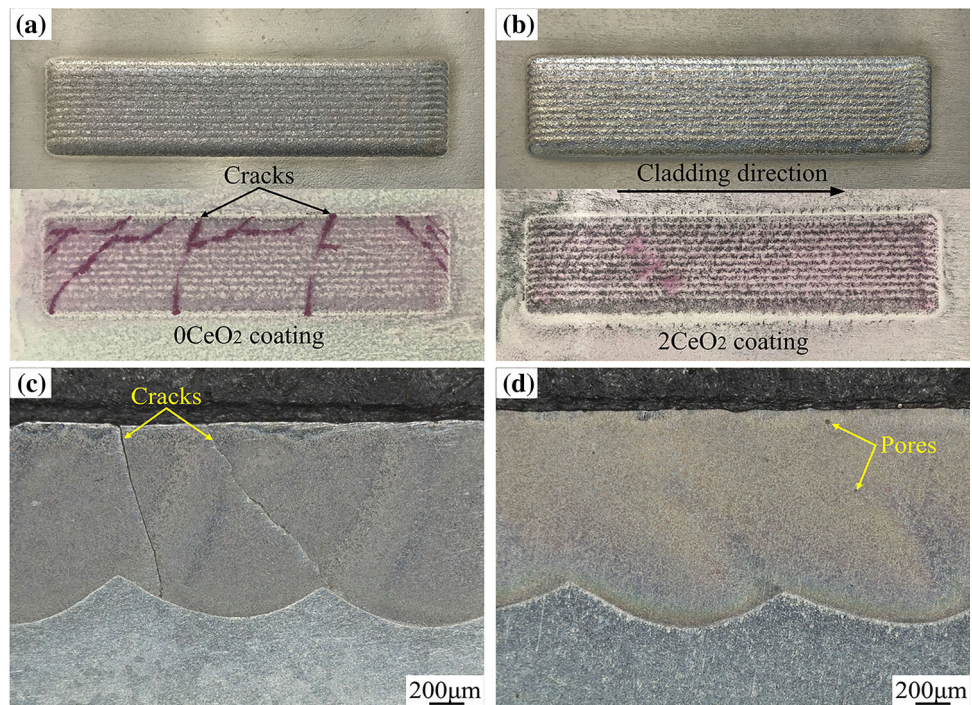


Fig. 6. XRD results of the coatings.

escape from the molten pool due to its extremely fast solidification speed; (b) the addition of CeO₂ enhanced the convective stirring ability of the molten pool, resulting in a small amount of gas involved in the molten pool. Meanwhile, it can also be seen in Fig. 5(c) and (d) that the fusion line of the coatings presented a obvious wave-like transition. The reason is that the laser energy in the laser cladding process conforms to the Gaussian distribution, showing the phenomenon of more energy close to the center and less energy in the edge. Therefore, the laser energy absorbed in the bonding area was larger, increasing the substrate melting amount, which showed a convex feature in the bonding interface.

Phase Composition

Figure 6 shows the XRD results of the coatings with different CeO₂ content. From Fig. 6, it can be concluded that the CeO₂ had no obvious effect on the phase composition, and the coatings were mainly made up of TiC, TiB₂, Ti₂Ni and α-Ti. However, a slight diffraction peak of Ce₂O₃, Cr, Al and V was found in the 2CeO₂ coating. The formation of Ce₂O₃ was mainly due to the decomposition of CeO₂ (as shown in Eq 4) at high temperature (Ref 45); then, the Ce atoms reacted with the undecomposed CeO₂ to form Ce₂O₃ (as shown in Eq 5). Besides, the decomposition of CeO₂ also indicated that the reactive gas O₂ might remain in the 2CeO₂ coating and form the micro-pores (as shown in Fig. 5d). At the same time, it can be seen that the relative intensity of diffraction peak for Ti₂Ni was the highest, while TiC and TiB₂ were relatively low. It is noteworthy that the relative intensity of diffraction peak of α-Ti in 0CeO₂ coating was very low, and compared with 0CeO₂ coating, that in 2CeO₂ coating was further reduced.

During laser cladding, Ti-6Al-4V + Ni45 + NiCr-Cr₃-C₂ + CeO₂ cladding materials and the surface layer of Ti-6Al-4V melted simultaneously to form the high-temperature molten pool by reactions (1, 2, 3, 4 and 5), and then TiC, TiB₂, Ti₂Ni precipitated from the molten pool by reactions (6, 7 and 8), and finally, β-Ti was transformed into α-Ti through phase transformation (9).



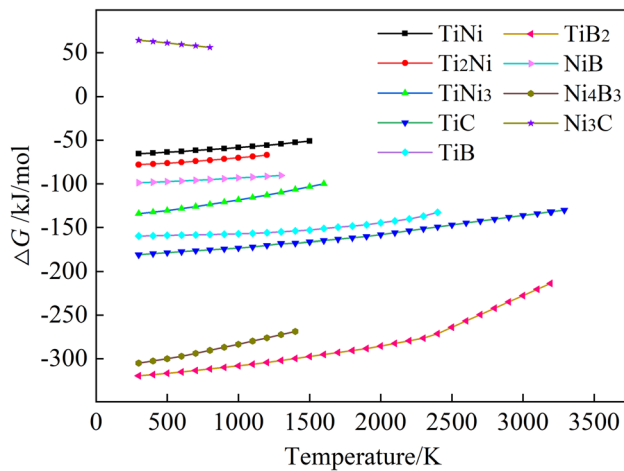
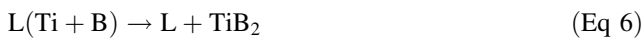
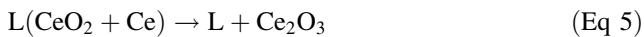


Fig. 7. Molar reaction Gibbs free energy curves (ΔG - T curve) of the compounds.



According to XRD, the possible compounds between Ti, Ni, C and B are mainly considered, including TiNi, Ti₂Ni, TiNi₃, TiC, TiB, TiB₂, Ti₃B₄, Ni₃C, NiB and Ni₄B₃. Based on the references (Ref 46), the molar reaction Gibbs free energy curves versus temperature (ΔG - T curve) of most of the above compounds are obtained, as shown in Fig. 7. As seen in Fig. 7, the ΔG of Ni₃C is always positive; thus, Ni₃C will not be generated spontaneously. Three kinds of Ti-Ni intermetallic compounds (TiNi, Ti₂Ni and TiNi₃) might be formed by the reaction between Ti and Ni, and their molar reaction Gibbs free energies are all negative; thus, all of them have a probability to generate spontaneously in the molten pool. Among them, TiNi₃ has the lowest ΔG and the highest possibility of spontaneous formation. However, it is pointed out that Ti₂Ni has the strongest crystal structure stability than TiNi₃ and TiNi (Ref 47), which might be the reasonable explanation for the formation of numerous Ti₂Ni precipitates in the coating. The ΔG of TiC is negative, and Ti has a good affinity with C (Ref 48); therefore, it is easy to in situ synthesize TiC. For the Ti₃B₄, the previous studies have proved that it was extremely difficult to form under the rapid cooling condition (Ref 49, 50). The ΔG of TiB₂ is lower than TiB; thus,

B reacts with Ti preferentially to form the metastable phase TiB₂. Additionally, there is not enough time for TiB₂ to react with Ti to form TiB during the rapid solidification process. Considering that the affinity between B and Ti is much higher than that between B and Ni, and B originates from Ni45 powders, and the content of B is only 2.38–3.85 wt.% in the cladding material system. Therefore, the possibility for the formation of Ni-B compounds (NiB and Ni₄B₃) by the reaction of extra B element with Ni element in molten pool is extremely low. As a consequence, TiC, TiB₂ and Ti₂Ni were finally formed in the coatings. Ceramic phases TiC, TiB₂ and intermetallic compound Ti₂Ni are typical coating hard reinforcing phases, which can remarkably improve the coating microhardness and tribological properties (Ref 51–53).

Microstructure

Based on the microstructure, the laser-clad coatings were divided into five typical regions: the cladding layer (CL), overlapping zone (OZ), bonding zone (BZ), heat-affected zone (HAZ) and substrate, as illustrated in Fig. 8. And where CL-1, CL-2, CL-3 are the three adjacent cladding tracks along the overlapping direction; OZ-1, OZ-2, OZ-3 correspond to the overlapping zone of CL-1, CL-2, CL-3, respectively; D is the depth of cladding layer; W is the width of heat-affected zone.

Figure 9 shows the microstructure of the coatings with different CeO₂ content at each cladding track in CL and OZ. It can be seen from the figure that the microstructure of the coatings at each cladding track in CL (CL-1, CL-2 and CL-3) and OZ (OZ-1, OZ-2 and OZ-3) was basically the same in this study. The coating microstructure was relatively coarse in CL, but fine and scattered in OZ. The specific reasons are as follows: During laser cladding, the heat accumulation could be occurred in the cladding layer, and the molten pool had a slow heat dissipation and long survival time, which is conducive to the microstructure growth. However, a new molten pool was formed due to the “reheating” effect of the next laser scanning in the overlapping process, and the microstructure in the overlapping zone re-nucleated and re-grew. The overlapping zone had a faster cooling rate because it was close to the previous unmelted cladding track. At the same time, the solid–liquid interface provided the heterogeneous nucleation substrate, resulting in a relatively high nucleation rate in the overlapping zone. In addition, the microstructure in this region would be refined to a certain extent due to the lack of enough time for the nucleus growing. It is worth noting that the “reheating” effect promoted the further dilution of the substrate to the coating, causing the scattered microstructure. For the microstructure of 0CeO₂ coating (see Fig. 9b), a large amount of dendritic phase

Fig. 8. Schematic diagram of the coating cross-sectional morphology.

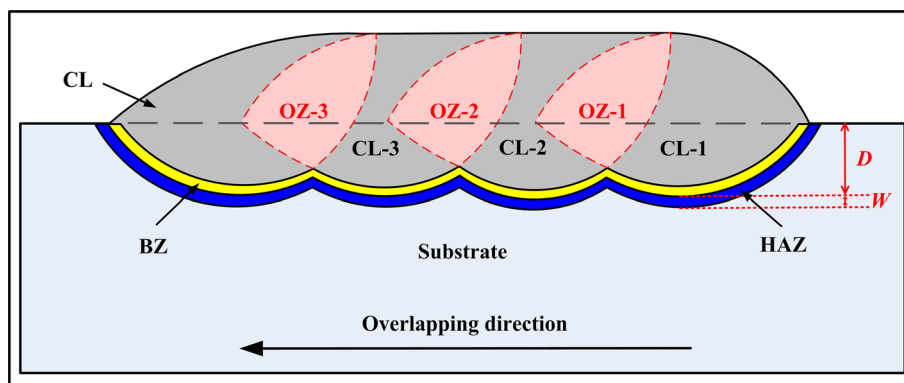


Table 4 EDS results of each phase in the coatings.

Spectrum	Fraction	Element composition								
		B	C	Al	Si	Ti	V	Cr	Fe	Ni
Point 1 (TiC)	wt.%	...	18.62	0.66	0.20	75.22	...	1.06	0.44	3.80
	at.%	...	47.77	0.75	0.22	48.39	...	0.63	0.24	2.00
Point 2 (TiB ₂)	wt.%	27.51	...	0.16	...	64.84	3.86	2.75	...	0.88
	at.%	62.87	...	0.14	...	33.44	1.87	1.31	...	0.37
Point 3 (TiC _x)	wt.%	...	12.38	2.05	0.68	69.07	1.11	3.86	0.99	9.86
	at.%	...	36.11	2.66	0.85	50.51	0.76	2.60	0.62	5.89
Point 4 (Ti ₂ Ni)	wt.%	...	1.48	1.26	0.52	58.34	2.89	6.36	2.80	26.35
	at.%	...	5.90	2.23	0.90	58.44	2.72	5.87	2.41	21.53
Point 5 (α-Ti)	wt.%	...	2.09	1.02	0.21	77.41	3.60	4.26	1.32	10.09
	at.%	...	7.98	1.73	0.34	74.01	3.24	3.76	1.07	7.87
Point 6 (TiC)	wt.%	...	17.87	0.54	0.22	77.65	...	0.77	...	2.95
	at.%	...	47.68	0.62	0.24	49.23	...	0.56	...	1.67
Point 7 (TiB ₂)	wt.%	26.35	64.70	4.26	3.89	...	0.80
	at.%	61.54	34.11	2.11	1.89	...	0.35
Point 8 (TiC _x)	wt.%	...	12.46	2.48	0.81	64.41	1.32	3.86	1.41	13.25
	at.%	...	36.38	3.22	1.01	47.10	0.91	2.60	0.88	7.90
Point 9 (Ti ₂ Ni)	wt.%	...	0.98	0.69	0.39	61.43	3.01	5.47	2.52	25.51
	at.%	...	3.97	1.26	0.68	62.64	2.88	5.14	2.21	21.22

(Point 1) and long rod-shaped phase (Point 2) with certain orientation characteristics were distributed on the exposed matrix phase (Point 5). The micron-spherical granular phase (Point 3) was clearly observed, and the irregular bulk-like phase (Point 4) formed the network grain boundary structure. From Fig. 9(e), the microstructure of 2CeO₂ coating was uniform and dense, and the coarse dendritic phase and long rod-shaped phase obviously disappeared. Instead, the coating was mainly composed of petal-shaped phase (Point 6), short rod-shaped phase (Point 7), micron-spherical granular phase (Point 8) and dense microporous irregular bulk-like phase (Point 9). The EDS results of each phase in the coatings are listed in Table 4. As seen in Table 4, the dendritic phase (Point 1) mainly contains Ti and C with the atomic ratio close to 1:1; the long rod-shaped phase (Point 2) and short rod-shaped phase

(Point 7) mainly contain Ti and B with the atomic ratio close to 1:2; the micron-spherical granular phase (Point 3 and Point 8) mainly contains Ti and C; the irregular bulk-like phase (Point 4 and Point 9) mainly contains Ti and Ni with the atomic ratio close to 2:1; the matrix (Point 5) primarily contains Ti, C, Al, Cr, V, Ni, Si and other elements, and the mass fraction of Ti element is more than 70 wt.%. Combined with XRD results, it can be determined that the phase of Point 1 was dendritic TiC, Point 6 was petal-shaped TiC, Point 3 and Point 8 were typical micron-spherical granular vacancy-type TiC_x, Point 2 and Point 7 were rod-shaped TiB₂, Point 4 and Point 9 were irregular bulk-like Ti₂Ni, Point 5 was continuous solid solution matrix α-Ti.

It can be seen from Fig. 9(b) and (e) that when 2 wt.% CeO₂ was added, the exposed surface area of matrix

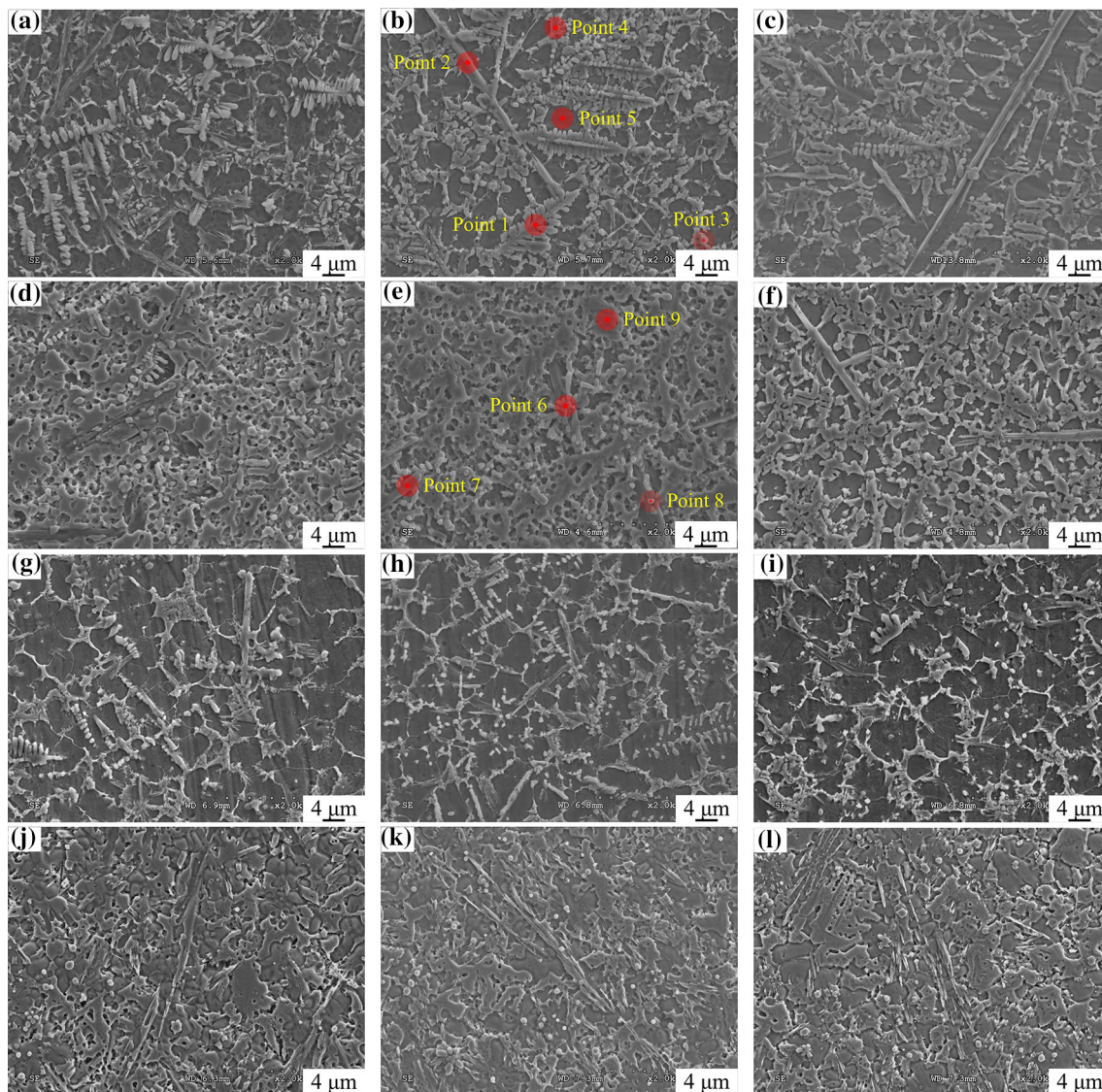


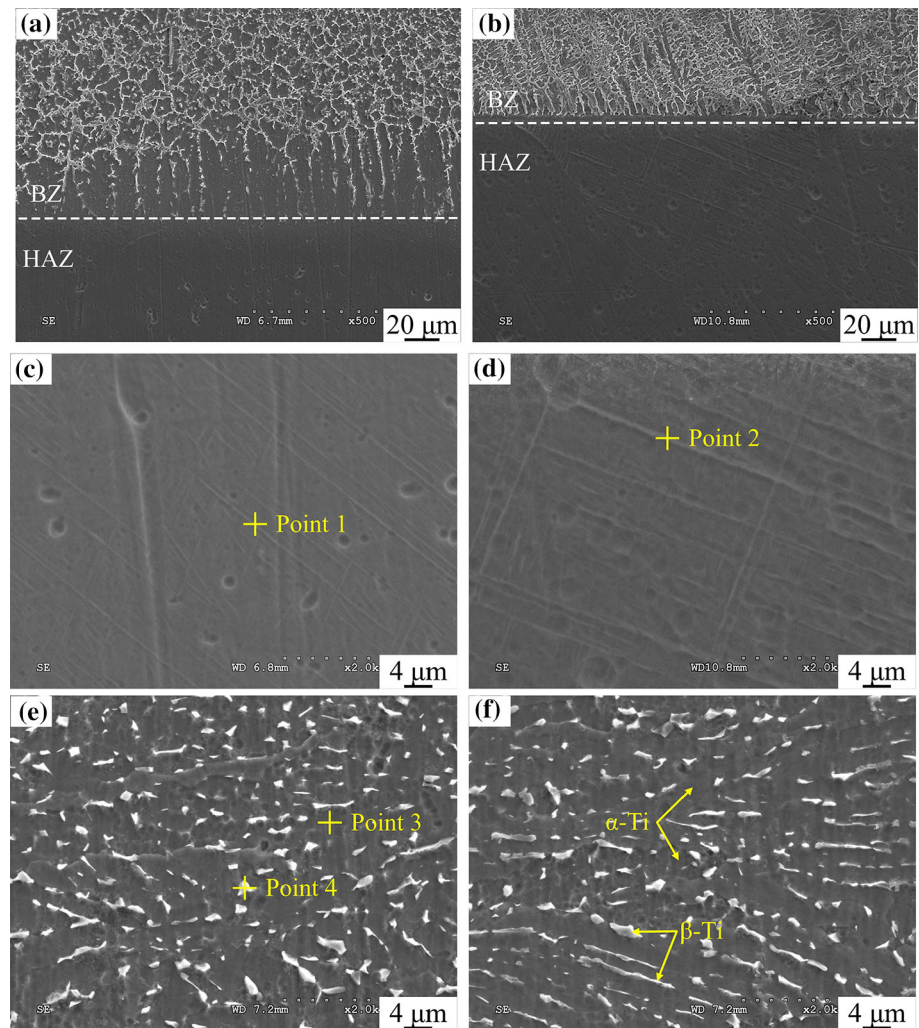
Fig. 9. Microstructure of the coatings with different CeO_2 content at each cladding track in CL and OZ: (a–c) microstructure of CL-1, CL-2, CL-3 in 0CeO_2 coating; (d–f) microstructure of CL-1, CL-2, CL-3

in 2CeO_2 coating; (g–i) microstructure of OZ-1, OZ-2, OZ-3 in 0CeO_2 coating; (j–l) microstructure of OZ-1, OZ-2, OZ-3 in 2CeO_2 coating.

decreased and the density of precipitated phase significantly increased, which was consistent with the XRD results. At the same time, the microstructure distribution became more uniform, and TiC changed from coarse dendrite to petal-shaped and granular, TiB_2 from long rod-shaped to short rod-shaped, and Ti_2Ni from irregular bulk-like to microporous irregular bulk-like, which indicated that the addition of CeO_2 significantly refined the microstructure and promoted its homogenization. The reason for the refinement of coating microstructure is that the Ce atoms generated by CeO_2 decomposition are grain boundary segregation elements, which will preferentially diffuse and segregate at grain boundaries and dislocations, reducing the Gibbs free energy of the system and the

driving force of grain growth, thus refining the microstructure (Ref 31, 54). Moreover, the special physical and chemical activity of Ce atoms can make it react with other substances to form high melting point compounds, which can become new nucleation particles to improve the nucleation rate and finally refine microstructure (Ref 31, 54, 55). From Fig. 9(b) and (e), the coarse dendritic TiC and long rod-shaped TiB_2 in the 0CeO_2 coating augmented the probability of crack initiation to a certain extent and increased the coating cracking tendency, which was consistent with the PT results. However, it is worth noting that the growth morphology of Ti_2Ni in the coating had changed significantly; the microporous structure could make up for the defects in mechanical properties and played a role

Fig. 10. Microstructure of the coatings with different CeO₂ content in BZ, HAZ and substrate: (a, c, e) microstructure of BZ, HAZ, substrate in 0CeO₂ coating; (b, d, f) microstructure of BZ, HAZ, substrate in 2CeO₂ coating.



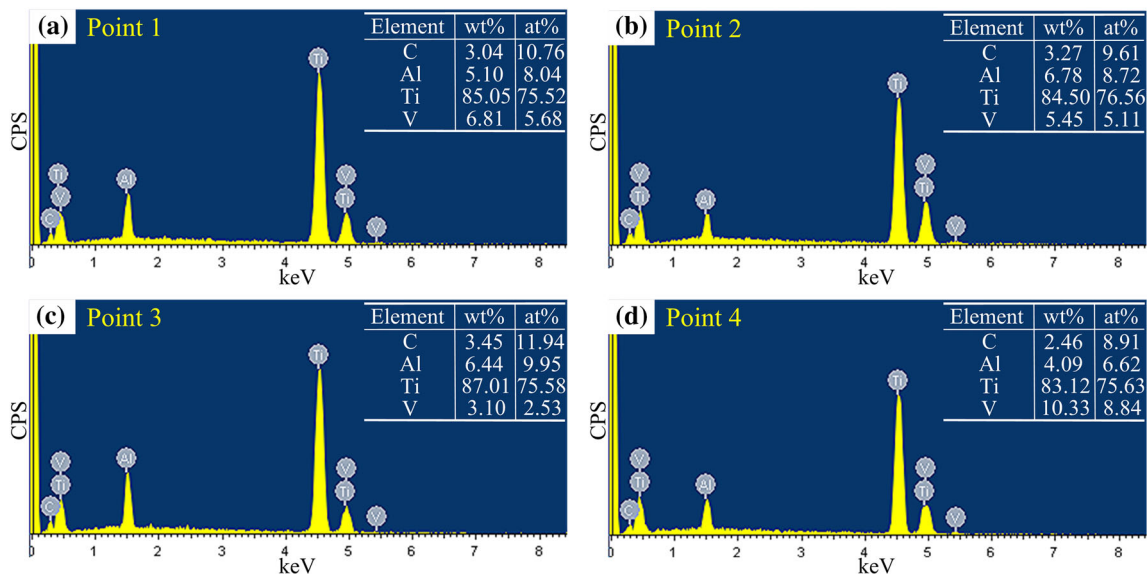
of buffering and decompression, which was conducive to minimize stress buildup and reduce the cracking tendency along the grain boundary, thus avoiding the initiation and propagation of coating cracks (Ref 56). Meanwhile, the high refinement and uniform distribution of TiC and TiB₂ also contributed to the reduction of stress concentration. Therefore, a crack-free coating with 2 wt.% CeO₂ was obtained.

Figure 10 shows the microstructure of the coatings with different CeO₂ content in BZ, HAZ and substrate. From Fig. 10(a) and (b), the coating microstructure of BZ was mainly in the form of planar crystal, which was perpendicular to the bonding interface. This is because the crystal morphology of BZ is mainly controlled by the ratio G/R (where G is the temperature gradient, and R is the crystal growth rate) (Ref 6). In the bonding zone, G is larger, R is smaller; thus, the G/R is relatively large (Ref 57). Therefore, according to the classical constitutional supercooling theory (Ref 58), the microstructure in the bonding zone was typical planar crystal, which exhibited the characteristics of

directional solidification. Meanwhile, it was found that the amount of TiC in the bonding zone obviously decreased. The explanations of this phenomenon are as follows: (a) BZ was close to the substrate, and the TiC was lacked of sufficient growth conditions due to the fast cooling rate. (b) The substrate had an obvious dilution effect on BZ; thus, the C content provided by Ti-6Al-4V was limited. (c) The relative atomic mass of B and C is smaller than Ni element; thus, Ni tended to be enriched in BZ during the convection of molten pool. Therefore, the C content of BZ was much lower than that of CL and OZ, which led to the insufficient growth driving force for TiC. From Fig. 10(c), (d), (e) and (f) and Fig. 11, it was found that the microstructure of HAZ was mainly the acicular martensite α' -Ti and its element composition was similar to that of $\alpha + \beta$ dual phase in the substrate zone. In the heating process of laser cladding, when the temperature of heat-affected zone was higher than 882.5 °C, α -Ti transformed into β -Ti by diffusion-type solid-state phase transformation (Ref 59). During the cooling process, when the temperature

Table 5 The depth of cladding layer and width of heat-affected zone for the laser-clad coatings at each cladding track.

Coatings	Depth of cladding layer/ μm				Width of heat-affected zone/ μm			
	CL-1	CL-2	CL-3	Standard deviation	HAZ-1	HAZ-2	HAZ-3	Standard deviation
Without CeO_2	761	733	756	14.93	327	341	328	7.81
2 wt.% CeO_2	777	795	782	9.29	359	355	364	4.51

**Fig. 11.** EDS image of each phase: (a) Point 1; (b) Point 2; (c) Point 3; (d) Point 4.

dropped to 1670 °C, β -Ti precipitated (Ref 59). Normally, as the temperature continued dropping to 882.5 °C, β -Ti would undergo solid-state phase transformation, and then α -Ti precipitated at the original grain boundary of β -Ti (Ref 59, 60). However, the normal precipitation of α -Ti from β -Ti might not occur due to the extremely fast cooling rate of laser cladding in HAZ. Therefore, the diffusion-type solid-state phase transformation was inhibited, and β -Ti was transformed into acicular martensite α' -Ti with HCP structure by lattice shear manner. In addition, as the strong α -stabilizing element, the slight diffusion of C atoms in HAZ could promote the formation of acicular martensite α' -Ti. Furthermore, it was difficult to distinguish α -Ti from metastable phase α' -Ti by XRD, given the same lattice type and lattice constant (Ref 61). It was worth pointing out that the atomic radius of Al, V and other alloy elements dissolved in acicular martensite α' -Ti was smaller than that of Ti, resulting in little lattice distortion, which would not have a significant improvement for the coating hardness.

Table 5 shows the depth of cladding layer and width of heat-affected zone for the laser-clad coatings at each cladding track. It can be clearly observed that the depth of CL-1, CL-2, CL-3 of 0CeO₂ and 2CeO₂ coating was 761,

733, 756, 77, 795 and 782 μm , respectively. It can draw a conclusion that the depth of cladding layer increased when added 2 wt.% CeO₂. This phenomenon verified that the addition of CeO₂ could increase the laser energy absorption of the cladding material (Ref 62, 63), which implied that additional energy input was provided indirectly. Moreover, the surface active element Ce could drive the convection center of the molten pool to move toward the substrate (Ref 64). Hence, more substrate was melted and caused larger depth of the cladding layer. In addition, the standard deviation of the depth of cladding layer for 2CeO₂ coating was smaller than that of 0CeO₂ coating, which indicated that CeO₂ could promote the homogenization of the depth of cladding layer. The variation of width of heat-affected zone had a similarity to that of cladding layer.

Figure 12 shows the mapping surface scanning results of micro-area in 0CeO₂ coating and Ti-C binary alloy phase diagram. From Fig. 12(a), (b), (c) and (d), the C-rich area was mainly distributed in the form of coarse dendritic phase (A1) and micron-spherical granular phase (A3). Combined with XRD, SEM and EDS, it can be determined that A1 was the dendritic TiC and A3 was vacancy-type TiC_x. The final morphology of TiC in the coating is related

Table 6 EPMA point analysis of the white particles.

Element	C	O	Al	Si	Ti	V	Cr	Fe	Ni	Ce
wt.%	0.320	12.857	0.604	0.231	7.687	0.792	1.483	0.527	5.163	70.336
at.%	1.4025	44.3279	1.2538	0.4810	16.3415	0.6492	1.4926	0.5914	4.9385	28.5216

Table 7 Crystallographic data of Ce₂O₃ and TiC (Ref 72, 73).

Compound	Structure	Space group	Lattice parameter, Å			Atomic position			
			<i>a</i>	<i>b</i>	<i>c</i>	Atom	<i>x</i>	<i>y</i>	<i>z</i>
Ce ₂ O ₃	Trigonal/rhombohedral	P-3M1	3.941	3.941	6.182	Ce	0.3333	0.6667	0.2481
						O	0.3333	0.6667	0.6447
						O	0	0	0
TiC	Cubic	FM-3M	4.3275	4.3275	4.3275	Ti	0.5	0.5	0.5
						C	0	0	0

to its crystal structure, thermodynamic and solidification conditions. Based on the Ti-C binary alloy phase diagram (Ref 59) (see Fig. 12l), TiC precipitates firstly through a homogeneous transformation of L → residual liquid phase (L1) + TiC. The molten pool is easily constitutionally supercooled due to the high liquidus slope of TiC, leading to the primary TiC growing up in the manner of dendrite and forming the residual liquid phase (L1) + TiC dendrite; furthermore, L1 provides the abundant space for TiC growth; thus, the TiC finally grows to be coarse dendrites. However, there are inevitably point defects, line defects and surface defects in the actual crystals, which make the atoms in TiC unable to occupy the ideal lattice node position strictly, thus forming a non-stoichiometric compound TiC_x (where *x* is the stoichiometric ratio of C and Ti), i.e., vacancy-type titanium carbide. Some studies suggested that the value of *x* in vacancy-type titanium carbide should be in the range of 0.47 and 1.0 (Ref 65-67). In this study, the *x* of dendritic TiC and petal TiC is close to 1.0, which was considered as ideal TiC_x (*x* = 1). The main reason for the formation of vacancy-type TiC_x (*x* ≠ 1) in 0CeO₂ coating is that the diffusion ability of Ti and C atoms decreased as the temperature and the supercooling rate decreased; meanwhile, the driving force of nucleation and growth of TiC was weakened. Therefore, the micron-spherical granular vacancy-type TiC_x (*x* ≠ 1) was precipitated through low-temperature eutectic transformation and solid-phase transformation. Figure 12(a), (b), (c) and (e) shows that B element mainly distributed in the coating in the form of short rod-shaped and circular spot-like crystals. Combined with Fig. 9(b), it is clear that the long rod-shaped phase was TiB₂. In fact, the B-rich circular spot-like phase was also long rod-shaped TiB₂, but having a certain angle with the observation surface of the coating.

TiB₂ has the hexagonal close-packed (HCP) structure, which is easy to grow preferentially along the *c*-axis in the crystallization process and finally forms a rod-shaped structure (Ref 68). Figure 12(a), (b), (c), (g), (h), (j) and (k) presents that the distribution of Al, Cr, Fe and Si was coincident approximately with that of Ni element. Combined with XRD, SEM and EDS, Ni primarily existed in the form of Ti₂Ni grain boundary structure and solid solution in α-Ti matrix. Therefore, Al, Cr, Fe and Si had a certain strengthening effect on the grain boundary and matrix.

Figure 13 shows the quantitative results of micro-area element distribution in 2CeO₂ coating by EPMA. As seen in Fig. 13(l), numerous white particles distributed uniformly in the coating from the backscattered electron image. The EPMA point analysis results (see Table 6) show that the white particles were mainly made up of Ce and O elements with the atomic ratio close to 2:3. Combined with Fig. 13(j) and (k), XRD and EDS, the white particles can be determined as Ce₂O₃, which also verified the thermal decomposition of CeO₂. It can be seen from Fig. 13(a) and (b) that C element distributed uniformly in the coating in the form of petal-shaped and granular crystals, which corresponded to petal-shaped and granular TiC_x in Fig. 9(e). Figure 13(a) and (c) shows that B element was mainly distributed in the coating in the form of short rod-shaped and circular spot-like crystals. Combined with Fig. 9(e), the short rod-shaped phase was considered as TiB₂. In fact, the B-rich circular spot-like phase was also short rod-shaped TiB₂ as aforementioned. From Fig. 13(d), (e), (f), (h) and (i), Al, Cr, Fe and Si distributed basically consistent with that of Ni element. Based on XRD and EDS, Ni mainly existed in the form of microporous irregular bulk-like Ti₂Ni or dissolved in α-Ti matrix, indicating

Fig. 12. Mapping surface scanning results of micro-area in 0CeO_2 coating: (a) SEM, (b) EDS-layered electronic image, (c) Ti, (d) C, (e) B, (f) Ni, (g) Al, (h) Cr, (i) V, (j) Fe, (k) Si, (l) Ti-C binary alloy phase diagram.

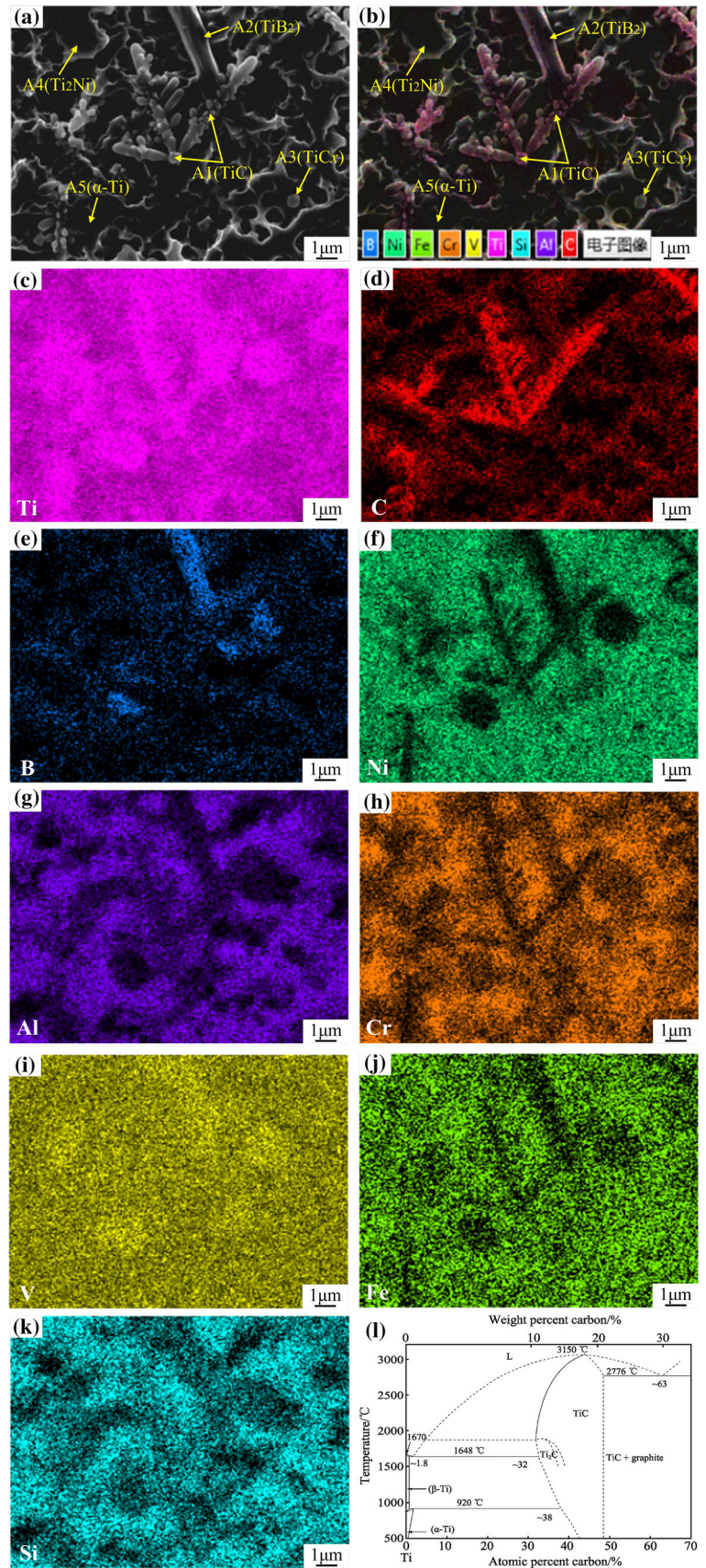


Table 8 Bramfitt’s planar lattice disregistry calculation of Ce₂O₃ and TiC.

Matching faces	(10 $\bar{1}$ 0)Ce ₂ O ₃ //(110)TiC		
$[uvw]_{Ce_2O_3}^i$	[0001]	$[\bar{1}2\bar{1}0]$	$[\bar{1}2\bar{1}1]$
$[uvw]_n^i$	$[\bar{1}10]$	[001]	$[\bar{1}11]$
$\theta, ^\circ$	0	0	2.747
$d_{[uvw]_{Ce_2O_3}^i}, \text{Å}$	6.182	3.941	7.331
$d_{[uvw]_n^i}, \text{Å}$	6.116	4.325	7.491
$\delta, \%$	4.00		

that Al, Cr, Fe and Si had a strengthening effect on Ti₂Ni and α -Ti matrix. Combined with XRD, the existence of Cr, Al and V precipitates might be attributed to their limited solid solubility in the Ni matrix. Moreover, Fig. 13(c), (d) and (h) shows that the distribution of V was different from that of Ni, except for the overlapping areas, the distribution characteristics of V-rich area and B-rich area were basically consistent, indicating that V was segregated on the short rod-shaped TiB₂ surface. Among them, Ni, Cr, V, Fe and Si belong to β -stabilizing elements (Ref 61, 69, 70). It was reported that a relatively high content of β -stabilizing elements would increase the resistance of lattice transformation, but laser cladding provided a large supercooling degree, which contributed to the martensitic transformation of the β -Ti. Interestingly, according to Fig. 13(a), (b), (c), (j), (k) and (l), the white Ce₂O₃ particles were mainly distributed around TiC, which might show that Ce₂O₃ could be used as the nucleation substrate to refine TiC.

Planar Lattice Disregistry Calculation of Ce₂O₃ and TiC

At present, the rare earth oxides are widely considered as an effective refiner for laser cladding. However, whether Ce₂O₃ can be used as the effective nucleation substrate to trigger TiC heterogeneous nucleation still needs to be evaluated by means of Bramfitt’s planar lattice disregistry theory (Ref 71). The definition of Bramfitt’s planar lattice disregistry theory is as follows (Ref 71):

$$\delta_{(hkl)_n}^{(hkl)_s} = \frac{1}{3} \sum_{i=1}^3 \frac{|d_{[uvw]_s^i} \cos \theta - d_{[uvw]_n^i}|}{d_{[uvw]_n^i}} \times 100\% \quad (\text{Eq 10})$$

where $(hkl)_s$ is the low-index crystal plane of the substrate, $(hkl)_n$ is the low-index crystal plane of the nucleation phase, $[uvw]_s^i$ is the low-index direction in $(hkl)_s$, $[uvw]_n^i$ is the low-index direction in $(hkl)_n$, $d_{[uvw]}$ is the interatomic

spacing along $[uvw]$, θ is the angle between $[uvw]_s^i$ and $[uvw]_n^i$, δ is the planar lattice disregistry.

Figure 14(a) and (b) shows the crystal structure model of Ce₂O₃ and TiC. The crystallographic data of Ce₂O₃ and TiC (Ref 72, 73), and Bramfitt’s planar lattice disregistry calculation are listed in Table 7 and Table 8, respectively. Figure 15 shows the crystallographic relationship of Ce₂O₃ and TiC.

From the above calculation results, the planar lattice disregistry δ between the interface (10 $\bar{1}$ 0) of Ce₂O₃ and the interface (110) of TiC is 4.00%. According to Bramfitt’s planar lattice disregistry theory, when δ is less than 6%, heterogeneous nucleation is the most effective; thus, Ce₂O₃ can be used as nucleation substrate to refine primary TiC effectively, which has the fine grain strengthening effect. In addition, the relatively low disregistry shows that TiC and Ce₂O₃ are easier to form a coherent interface, which is conducive to the mutual matching of atoms at the interface (Ref 74, 75); therefore, the bonding between the two phases is firmer. Simultaneously, it is beneficial to release the interface stress, thus reducing the residual stress in the coating and improving the coating forming quality and mechanical performance.

It is complex to refine the microstructure of laser-clad coating by rare earth modification, which is not only related to the ability of refining microstructure as nucleation substrate, but also closely related to the crystal structure and distribution characteristics of precipitates and solute conditions. In this study, it was just proved that Ce₂O₃ could be used as nucleation substrate to refine TiC based on the Bramfitt’s planar lattice disregistry theory. However, we hope that this work can offer some experimental and theoretical basis for the refinement mechanism of Ce₂O₃.

Microhardness

Figure 16 illustrates the coating microhardness curves. As shown in Fig. 16(a), the microhardness of non-overlapping zone could be divided into four regions: cladding layer (CL), bonding zone (BZ), heat-affected zone (HAZ) and substrate. The average microhardness of 0CeO₂ coating was 827 HV₁, about 1.30 times higher than that of the substrate (359 HV₁). The average microhardness of 2CeO₂ coating was 993 HV₁, and the coating microhardness fluctuated more slightly than 0CeO₂ coating. The improvement of the coating microhardness was mainly attributed to the following aspects: (a) Numerous TiC, TiB₂ and Ti₂Ni reinforcing phases were in-situ synthesized, which improved the coating microhardness. (b) Al, Cr, V, Ni, Si and Fe had a strengthening effect. (c) The addition of CeO₂ could significantly refine the microstructure and

Fig. 13. EPMA element distribution of 2CeO_2 coating. (a) Ti, (b) C, (c) B, (d) Ni, (e) Al, (f) Cr, (g) V, (h) Fe, (i) Si, (j) Ce, (k) O, (l) backscattered electron image.

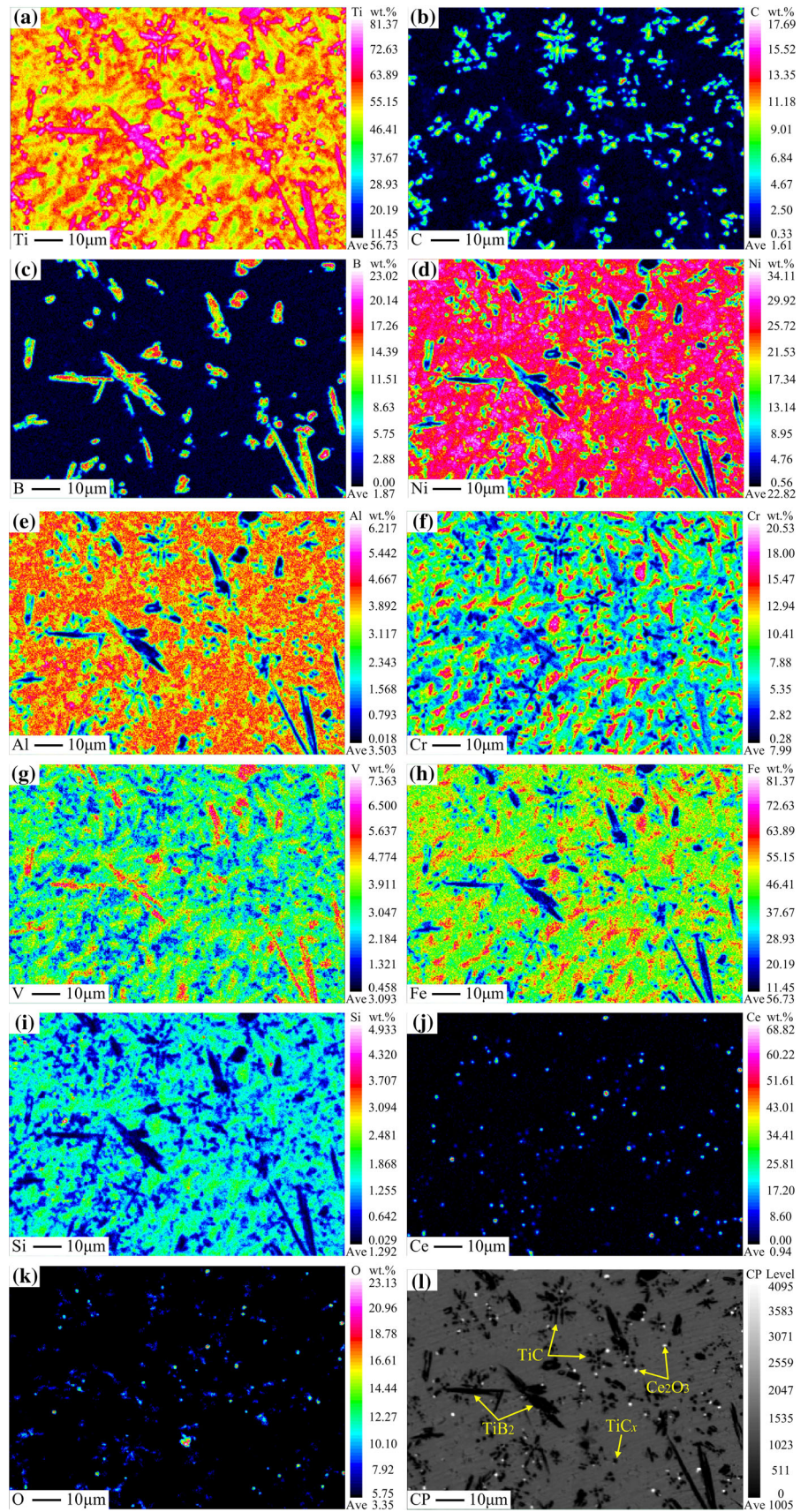


Fig. 14. Crystal structure model of Ce_2O_3 and TiC: (a) Ce_2O_3 , (b) TiC.

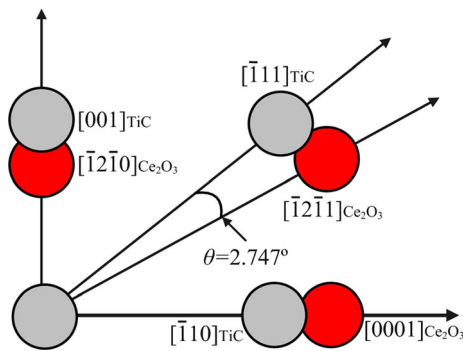
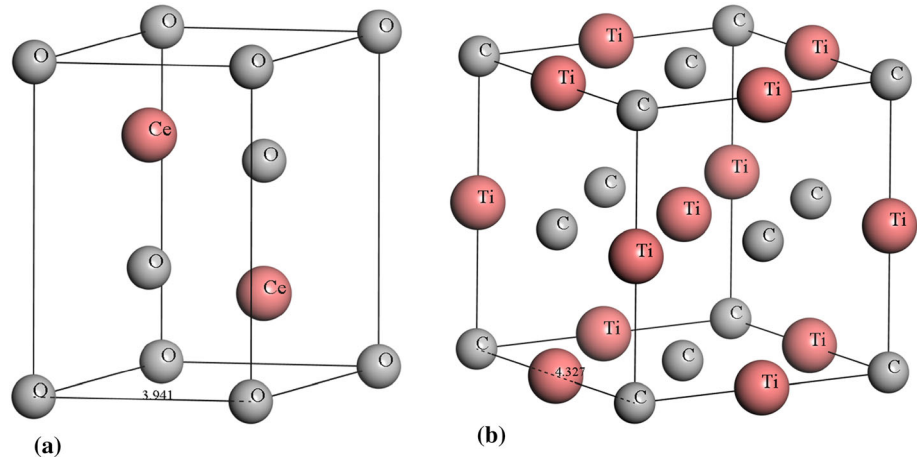


Fig. 15. Crystallographic relationship of Ce_2O_3 and TiC.

promote the microstructural homogeneity, thus further improving the microhardness and its distribution uniformity. It can also be seen that the microhardness of HAZ was only slightly higher than that of the substrate, indicating that the weak strengthening effect of acicular martensite α' -Ti. Dumas et al. (Ref 76) mentioned that the combination of ductile α' -Ti with α -Ti phase was considered to be the origin of the work-hardening of dual-phase titanium alloys, but the hardness of martensite α' -Ti was slightly higher or close to that of α -Ti (Ref 77); thus, the ability of heat treatment to improve the hardness of Ti-6Al-4V alloy was limited. As a contrast, the martensite α' -Ti in titanium alloy could not significantly improve the strength and hardness as martensite in steel. As shown in Fig. 16(b), the average microhardness of OZ-1, OZ-2, OZ-3 for 0CeO_2 and 2CeO_2 coatings was 814 HV_1 , 815 HV_1 , 809 HV_1 and 980 HV_1 , 983 HV_1 , 979 HV_1 , respectively, but slightly lower than those of CL. The decrease in hardness of OZ was mainly attributed to the competition between microstructure and dilution. The finer microstructure was beneficial to improving the hardness. However, the dilution of the substrate to the coating increased by the “reheating” effect, which decreased the hardness of OZ. Therefore, when dilution was dominant, the microhardness of OZ

decreased. Moreover, the microhardness distribution uniformity of OZ for 2CeO_2 coating was still better than that of 0CeO_2 coating.

Tribological Properties

Figure 17 illustrates the white light interference wear morphologies of the substrate and coatings. The wear pit of the substrate was larger and deeper than that of the coatings. The maximum wear depth of 0CeO_2 coating ($62.3 \mu\text{m}$) was lower than that of the substrate ($100.8 \mu\text{m}$), and that of 2CeO_2 coating was the lowest. Figure 18(a) and (b) shows the wear volume and friction coefficient curves of substrate and coatings, respectively. From Fig. 18(a), the wear volume of 0CeO_2 coating was $61.42 \times 10^{-3} \text{ mm}^3$, about 2.54 times lower than that of the substrate ($153.81 \times 10^{-3} \text{ mm}^3$), and that of 2CeO_2 coating ($42.40 \times 10^{-3} \text{ mm}^3$) was the smallest. Therefore, the wear resistance of 2CeO_2 coating is the best. Based on the well-known Archard wear model (Ref 78), when the sliding distance and normal load remain constant, the wear volume is inversely proportional to the hardness, that is, the lower the microhardness is, the larger the wear volume is, which is consistent with the microhardness tests. As shown in Fig. 18(b), under the same wear test conditions, the average friction coefficient of the substrate (0.349) was much lower than that of 0CeO_2 (0.425) and 2CeO_2 (0.354) coatings, which indicated a better anti-friction performance of the substrate. This phenomenon may be due to the large amount of heat generated by friction and rolling in the process of periodic wear of the substrate and coatings, which is easy to form titanium oxide TiO_x on the contact surface. Gardos et al (Ref 79) pointed that TiO_x had good self-lubricating properties; thus, the formation of TiO_x could significantly reduce the friction coefficient. However, the random distribution of coarse dendritic TiC, long rod-shaped TiB_2 and irregular bulk-like Ti_2Ni in 0CeO_2 coating led to the

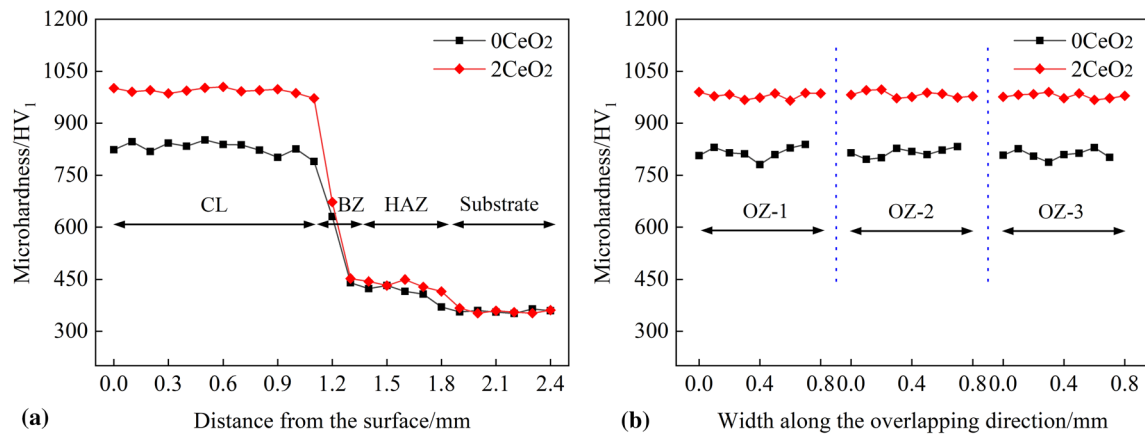


Fig. 16. Microhardness curves: (a) microhardness of non-overlapping zone, (b) microhardness of overlapping zone.

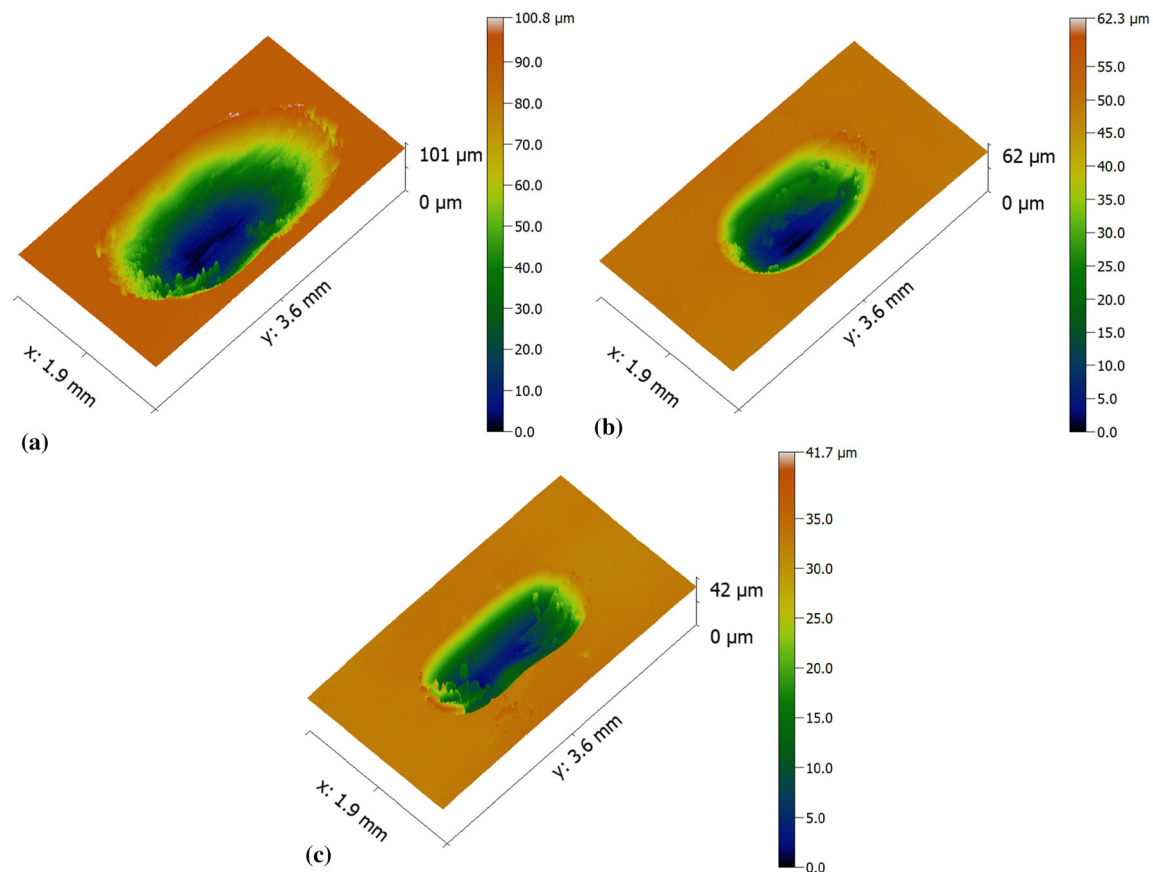


Fig. 17. White light interference wear morphologies of the Ti-6Al-4V substrate and coatings: (a) substrate, (b) 0CeO₂ coating, (c) 2CeO₂ coating.

unstable coating performance, which was easy to induce the stress concentration. As a result, the crack initiation and propagation were probably to occur in the lubrication film and finally would destroy the TiO_x lubrication film formed on the contact surface, which made the lubrication film instable. Therefore, the friction coefficient of the 0CeO₂ coating is higher than that of the substrate. Meanwhile, the

microstructure in 2CeO₂ coating was more uniform and dense. Moreover, the size of microporous Ti₂Ni of 2CeO₂ coating was approximately in the range of 1–8 μm, which provided living space for the retention of TiO_x and abrasive particles. Through frictional heating, the solid lubricant TiO_x softened, deformed and was extruded on the contact surface to form the lubrication film or preserved in Ti₂Ni

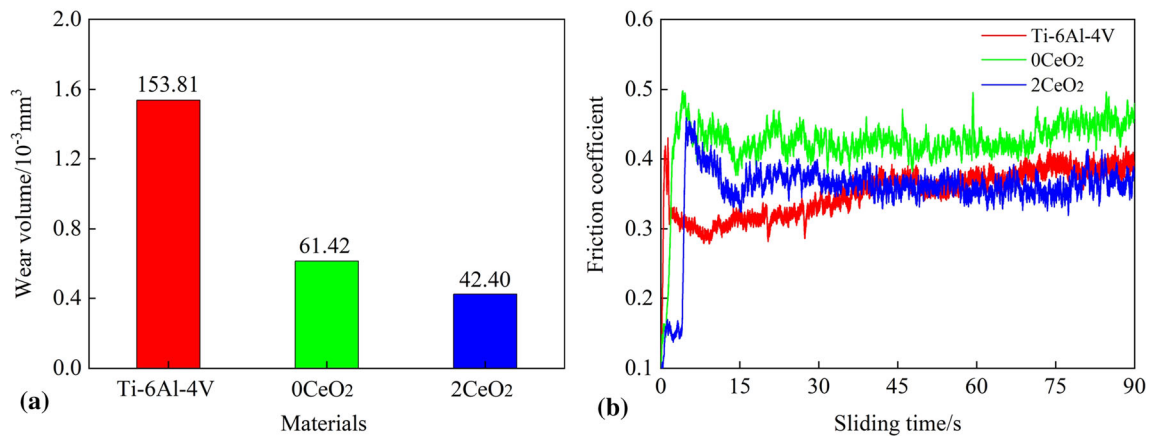


Fig. 18. Wear volume and friction coefficient curves of the substrate and coatings: (a) wear volume, (b) friction coefficient curves.

micropores. When the TiO_x lubrication film existed on the contact surface, the friction mainly occurred between the lubrication film and the counterpart (WC ball). As the lubrication film was gradually consumed, Ti_2Ni , TiC and TiB_2 , which played a role of “skeleton”, began to be worn. Simultaneously, the preserved TiO_x was extruded out of the micropores, and a lubrication film was reformed to reduce the friction. Therefore, the “Formation–Consumption–Reformation” mechanism of TiO_x lubrication film for 2CeO_2 coating was helpful to reduce the damage of the TiO_x lubrication film and was beneficial to its homogeneous spreading; thus, the friction coefficient of 2CeO_2 coating is lower than that of 0CeO_2 coating.

Figure 19 shows the wear surface morphology of the substrate and coatings. Figure 19(a), (d), (g) and (j) indicates that the surface of substrate was seriously worn, and the wear surface was uneven and rough with many deep grooves and clearly visible delamination. At the same time, due to the periodic change of the stress during the wear test, the Ti-6Al-4V substrate surface was pulled up, and a large area of spalling occurred on the wear surface, accompanied by obvious plastic deformation. Hence, the wear mechanism of the substrate was severe abrasive wear pattern and adhesive wear pattern. For the 0CeO_2 coating shown in Fig. 19(b), (e), (h) and (k), it was noted that the coating wear surface was relatively smooth, the grooves were shallow and the spalling phenomenon was obviously weakened. Moreover, there was a large amount of debris agglomerating on the coating wear surface. Therefore, the 0CeO_2 coating exhibited an abrasive wear pattern. Figure 19(c), (f), (i) and (l) shows that the wear surface was smoother, the smaller powder-like wear debris on the 2CeO_2 coating wear surface was uniformly dispersed with no bulk-like spalls and plastic deformation, and there were numerous clearly visible and shallow grooves; thus, the coating exhibited a typical abrasive wear pattern. During the reciprocating sliding process against the WC ball, the

uniform reinforcing phases were extruded and rolled into finer powder-like abrasive particles; the continuous microporous Ti_2Ni structure provided the embedding space for the abrasive particles, alleviated the stress concentration at the wear interface and increased the stability of the coating performance. Therefore, the debris aggregation phenomenon was obviously weakened, and the main feature was the smaller and more uniform grooves. Compared with the substrate, the coatings had higher microhardness, which greatly reduced the plowing effect of the WC ball on the coatings. Meanwhile, the addition of CeO_2 refined the microstructure, improved the uniformity of microstructure and reduced the cracking sensitivity, thus significantly ameliorating the wear resistance of 2CeO_2 coating.

Conclusions

1. Ni-based laser-clad coatings were successfully fabricated on Ti-6Al-4V alloy by Ti-6Al-4V + Ni45 + NiCr-Cr₃C₂ + CeO₂ mixed powders. The addition of CeO₂ had no obvious effect on the phase composition of the coatings, which mainly included TiC, TiB₂, Ti₂Ni and α -Ti, but Ce₂O₃ was found in 2CeO_2 coating.
2. With the addition of CeO₂, the coating surface cracks were effectively eliminated, but the micro-pores appeared. The coating microstructure was significantly refined, uniform and dense, and the exposed surface area of matrix decreased. Uniformly dispersed Ce₂O₃ particles formed by the decomposition of CeO₂ in the coating were mainly distributed around TiC.
3. The planar lattice discrepancy δ between the interface (10 $\bar{1}$ 0) of Ce₂O₃ and the interface (110) of TiC was 4.00%, and Ce₂O₃ could be used as the nucleation substrate to effectively refine the TiC.

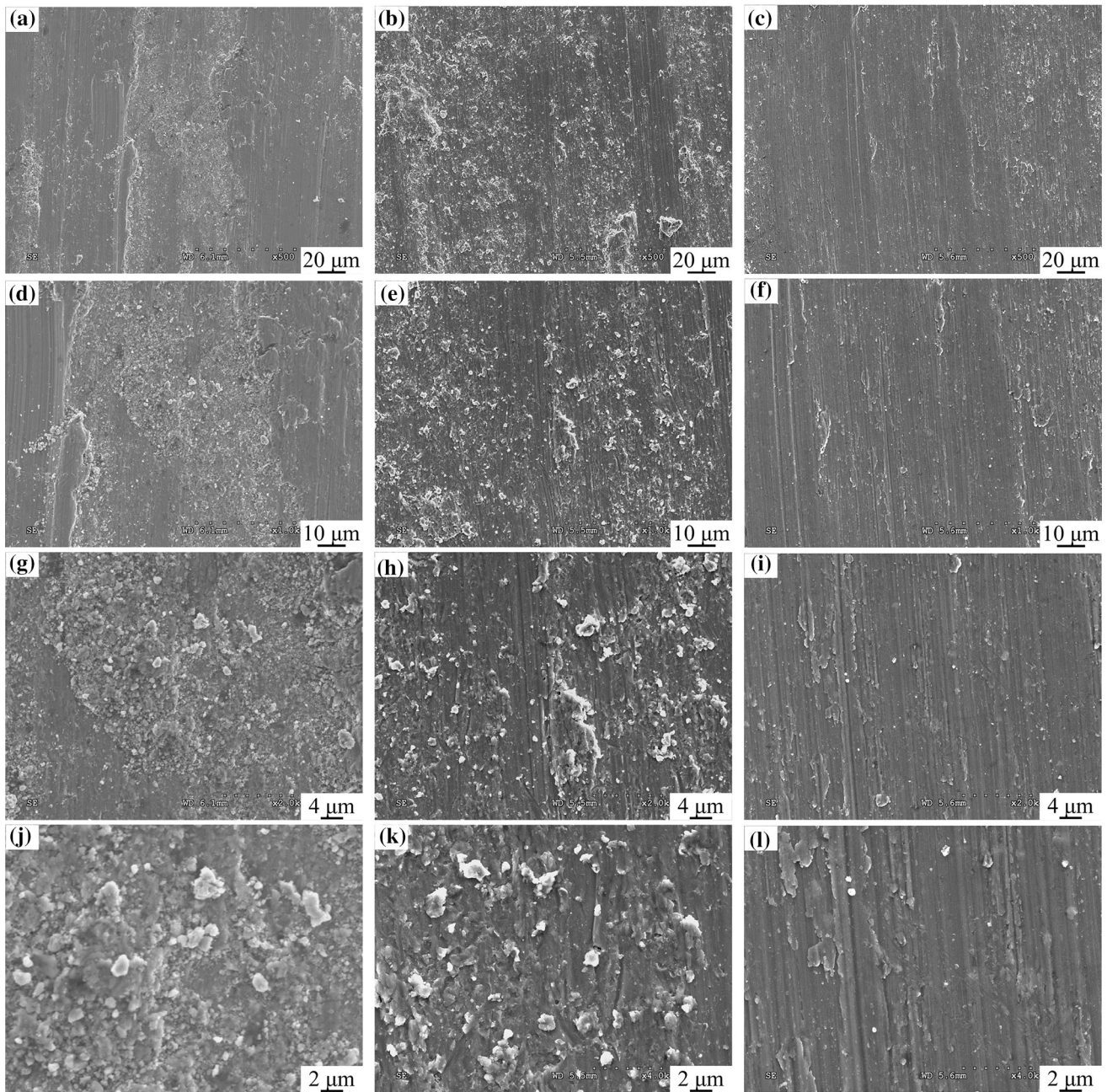


Fig. 19. Wear surface morphology of the substrate and coatings: (a, d, g, j) substrate, (b, e, h, k) 0CeO_2 coating, (c, f, i, l) 2CeO_2 coating.

4. With the addition of CeO_2 , the microhardness was increased, and the wear volume and friction coefficient were decreased. The wear resistance of the coatings was remarkably higher than the substrate. 2CeO_2 coating exhibited the best wear resistance and anti-friction properties compared with 0CeO_2 coating and exhibited an abrasive wear pattern.

Acknowledgments This work was supported by the Fundamental Research Funds for the Central Universities (Grant No.

3122018D013), the Fundamental Research Funds for the Central Universities (Grant No. 3122019069), the Tianjin Research Innovation Project for Postgraduate Students (Grant No. 2019YJSS077), the Science and Technology Innovation Fund for Postgraduate Students of the Civil Aviation University of China (Grant No. 201904).

References

1. P. Vo, E. Irissou, J.G. Legoux and S. Yue, Mechanical and Microstructural Characterization of Cold-Sprayed Ti-6Al-4V

- After Heat Treatment, *J. Therm. Spray Technol.*, 2013, **22**, p 954–964.
2. I. Hacisalihoglu, A. Samancioglu, F. Yildiz, G. Purcek and A. Alasaran, Tribocorrosion Properties of Different Type Titanium Alloys in Simulated Body Fluid, *Wear*, 2015, **332–333**, p 679–686.
 3. Y.H. Lin, Y.P. Lei, X.Q. Li, X.H. Zhi and H.G. Fu, A Study of TiB₂/TiB Gradient Coating by Laser Cladding on Titanium Alloy, *Opt. Lasers Eng.*, 2016, **82**, p 48–55.
 4. H. Paydas, A. Mertens, R. Carrus, J. Lecomte-Beckers and J. Tchoufang Tchoufang, Laser Cladding as Repair Technology for Ti-6Al-4V Alloy: Influence of Building Strategy on Microstructure and Hardness, *Mater. Des.*, 2015, **85**, p 497–510.
 5. A. Wank, B. Wielage, H. Podlesak, K.J. Matthes and G. Kolbe, Protection of Ti6Al4V Surfaces by Laser Dispersion of Diborides, *J. Therm. Spray Technol.*, 2005, **14**(1), p 134–140.
 6. Y.X. Chen, D.J. Wu, G.Y. Ma, W.F. Lu and D.M. Guo, Coaxial Laser Cladding of Al₂O₃-13%TiO₂ Powders on Ti-6Al-4 V Alloy, *Surf. Coat. Technol.*, 2013, **228**, p S452–S455.
 7. J.T.M.D. Hosson, Surface and Interface Engineering, *Int. J. Mater. Res.*, 1997, **100**(10), p 1279–1280.
 8. Y. You, J.H. Yan and M.F. Yan, Atomistic Diffusion Mechanism of Rare Earth Carburizing/Nitriding on Iron-Based Alloy, *Appl. Surf. Sci.*, 2019, **484**(1), p 710–715.
 9. R. Vilar, Laser Cladding, *J. Laser Appl.*, 1999, **11**(2), p 385–392.
 10. Y.T. Zhao, M.Y. Lu, Z.Q. Fan, P. McCormick, Q.Y. Tan, N. Mo and H. Huang, Microstructures and Mechanical Properties of Wear-Resistant Titanium Oxide Coatings Deposited on Ti-6Al-4V Alloy Using Laser Cladding, *J. Eur. Ceram. Soc.*, 2020, **40**(3), p 798–810.
 11. E. Toyserkani, A. Khajepour and S.F. Corbin, *Laser Cladding*, CRC Press, Boca Raton, 2004.
 12. M. Tsujikawa, D. Yoshida, N. Yamauchi, N. Ueda and T. Sone, Surface Modification of SUS304 Stainless Steel Using Carbon Push-Ahead Effect by Low Temperature Plasma Nitriding, *Mater. Trans.*, 2005, **46**(4), p 863–868.
 13. R. Bayón, A. Igartua, X. Fernández, R. Martínez and J. Damborenea, Corrosion-Wear Behaviour of PVD Cr/CrN Multilayer Coatings for Gear Applications, *Tribol. Int.*, 2009, **42**(4), p 591–599.
 14. J.H. Ouyang, S. Nowotny, A. Richter and E. Beyer, Characterization of Laser Clad Ytria Partially-Stabilized ZrO₂ Ceramic Layers on Steel 16MnCr5, *Surf. Coat. Technol.*, 2001, **137**(1), p 12–20.
 15. P.J. Callus and C.C. Berndt, Relationship Between the Mode II Fracture Toughness and Microstructure of Thermal Spray Coatings, *Surf. Coat. Technol.*, 1999, **114**(2), p 114–128.
 16. X.M. Li, Y.Y. Yang, T.M. Shao, Y.S. Jin and G. Barbezat, Impact Wear Performances of Cr₃C₂-NiCr Coatings by Plasma and HVOF Spraying, *Wear*, 1997, **202**(2), p 208–214.
 17. F. Weng, C.Z. Chen and H.J. Yu, Research Status of Laser Cladding on Titanium and Its Alloys: A Review, *Mater. Des.*, 2014, **58**, p 412–425.
 18. J.J. Dai, J.Y. Zhu, C.Z. Chen and F. Weng, High Temperature Oxidation Behavior and Research Status of Modifications on Improving High Temperature Oxidation Resistance Of Titanium Alloys and Titanium Aluminides: A Review, *J. Alloys Compd.*, 2016, **685**, p 784–798.
 19. M. Erfanmanesh, R. Shoja-Razavi, H. Abdollah-Pour and H. Mohammadian-Semmani, Influence of Using Electroless Ni-P Coated WC-Co Powder on Laser Cladding of Stainless Steel, *Surf. Coat. Technol.*, 2018, **348**, p 41–54.
 20. X.B. Liu and H.M. Wang, Microstructure and Tribological Properties of Laser Clad γ /Cr₇C₃/TiC Composite Coatings on γ -TiAl Intermetallic Alloy, *Wear*, 2007, **262**(5–6), p 514–521.
 21. Q.W. Meng, L. Geng and B.Y. Zhang, Laser Cladding of Ni-Base Composite Coatings onto Ti-6Al-4V Substrates with Pre-placed B₄C+NiCrBSi Powders, *Surf. Coat. Technol.*, 2006, **200**(16–17), p 4923–4928.
 22. H. Yan, K.W. Liu, P.L. Zhang, J. Zhao, Y. Qin, Q.H. Lu and Z.S. Yu, Fabrication and Tribological Behaviors of Ti₃SiC₂/Ti₃Si₃/TiC/Ni-Based Composite Coatings by Laser Cladding for Self-lubricating Applications, *Opt. Laser Technol.*, 2020, **126**, p 106077.
 23. R.L. Sun, Y. Tang and X.J. Yang, Microstructure and Tribological Properties of In-Situ Synthesized TiB₂-TiC/Ni-Based Composite Coating by Laser Cladding, *Trans. Mater. Heat Treat.*, 2004, **25**(05), p 1000–1003.
 24. J. Li, X.J. Zhang, H.P. Wang and M.P. Li, Microstructure and Mechanical Properties of Ni-Based Composite Coatings Reinforced by In Situ Synthesized TiB₂+TiC by Laser Cladding, *Int. J. Miner. Metall. Mater.*, 2013, **20**(01), p 57.
 25. F. Wu, T. Chen, H.J. Wang and D.F. Liu, Effect of Mo on Microstructures and Wear Properties of In Situ Synthesized Ti(C, N)/Ni-Based Composite Coatings by Laser Cladding, *Materials*, 2017, **10**(9), p 1047.
 26. S.F. Zhou and X.Q. Dai, Laser Induction Hybrid Rapid Cladding of WC Particles Reinforced NiCrBSi Composite Coatings, *Appl. Surf. Sci.*, 2010, **256**(14), p 4708–4714.
 27. J.M.S. Sousa, F. Ratusznei, M. Pereira, R. Medeiros Castro and E.I.M. Curi, Abrasion Resistance of Ni-Cr-B-Si Coating Deposited by Laser Cladding Process, *Tribol. Int.*, 2019, **143**, p 106002.
 28. V. Fallah, M. Alimardani, S.F. Corbin and A. Khajepour, Impact of Localized Surface Preheating on the Microstructure and Crack Formation in Laser Direct Deposition of Stellite 1 on AISI 4340 Steel, *Appl. Surf. Sci.*, 2010, **257**(5), p 1716–1723.
 29. X. Wang, M. Zhang and S. Qu, Development and Characterization of (Ti, Mo)C Carbides Reinforced Fe-Based Surface Composite Coating Produced by Laser Cladding, *Opt. Laser Eng.*, 2010, **48**(9), p 893–898.
 30. Y. Huang and X. Zeng, Investigation on Cracking Behavior of Ni-Based Coating by Laser-Induction Hybrid Cladding, *Appl. Surf. Sci.*, 2010, **256**(20), p 5985–5992.
 31. Y.N. Liu, R.L. Sun, W. Niu, T.G. Zhang and Y.W. Lei, Effects of CeO₂ on Microstructure and Properties of TiC/Ti₂Ni Reinforced Ti-Based Laser Cladding Composite Coatings, *Opt. Lasers Eng.*, 2019, **120**, p 84–94.
 32. C.Q. Qi, X.H. Zhan, Q.Y. Gao, L.J. Liu, Y.Z. Song and Y.P. Li, The Influence of the Pre-placed Powder Layers on the Morphology, Microscopic Characteristics and Microhardness of Ti-6Al-4V/WC MMC Coatings During Laser Cladding, *Opt. Laser Technol.*, 2019, **119**, p 105572.
 33. L.F. Cai, Y.Z. Zhang and L.K. Shi, Microstructure and Formation Mechanism of Titanium Matrix Composites Coating on Ti-6Al-4V by Laser Cladding, *Rare Met.*, 2007, **26**(4), p 342.
 34. K.M. Zhang, J.X. Zou, J. Li, Z.S. Yu and H.P. Wang, Surface Modification of TC4 Ti alloy by Laser Cladding with TiC+Ti Powders, *Trans. Nonferrous Met. Soc. China*, 2010, **20**(11), p 2192–2197.
 35. F. Weng, H.J. Yu, C.Z. Chen, J.L. Liu and L.J. Zhao, Fabrication of Co-Based Coatings on Titanium Alloy by Laser Cladding with CeO₂ Addition, *Mater. Manuf. Process.*, 2016, **31**(11), p 1461–1467.
 36. Q.T. Li, Y.P. Lei and H.G. Fu, Laser Cladding In-Situ NbC Particle Reinforced Fe-Based Composite Coatings with Rare Earth Oxide Addition, *Surf. Coat. Technol.*, 2014, **239**, p 102–107.
 37. T. Zhao, X. Cai, S.X. Wang and S. Zheng, Effect of CeO₂ on Microstructure and Corrosive Wear Behavior of Laser-Cladded Ni/WC Coating, *Thin Solid Films*, 2000, **379**, p 128–132.

38. L. Ding and S.S. Hu, Effect of Nano-CeO₂ on Microstructure and Wear Resistance of Co-Based Coatings, *Surf. Coat. Technol.*, 2015, **276**, p 565–572.
39. K.L. Wang, Q.B. Zhang, M.L. Sun and Y.M. Zhu, Effect of Laser Surface Cladding of Ceria on the Wear and Corrosion of Nickel-Based Alloys, *Surf. Coat. Technol.*, 1997, **96**(2–3), p 267–271.
40. J.N. Li, C.Z. Chen and J.H. Hu, Effect of SiC/Nano-CeO₂ on Wear Resistance and Microstructures of Ti₃Al/γ-Ni Matrix Laser-Cladded Composite Coating on Ti-6Al-4V Alloy, *Surf. Interface Anal.*, 2012, **44**(5), p 559–564.
41. R. Shi and Y. Wang, Variant Selection During α Precipitation in Ti-6Al-4V Under the Influence of Local Stress—A Simulation Study, *Acta Mater.*, 2013, **61**(16), p 6006–6024.
42. P. Barriobero-Vila, J. Gussone, J. Haubrich, S. Sandlöbes, J. Cesar Da Silva, P. Cloetens, N. Schell and G. Requena, Inducing Stable α+β Microstructures During Selective Laser Melting of Ti-6Al-4V Using Intensified Intrinsic Heat Treatments, *Materials*, 2017, **10**(3), p 268.
43. P. Wu, H.M. Du, X.L. Chen, Z.Q. Li, H.L. Bai and E.Y. Jiang, Influence of WC Particle Behavior on the Wear Resistance Properties of Ni-WC Composite Coatings, *Wear*, 2004, **257**(1–2), p 142–147.
44. H. Huang, G.Y. Yuan, J. Tong and W.J. Ding, Microstructure and Mechanical Properties of As-Cast and Solution-Treated Mg-Zn-Gd-Based Alloys Reinforced with Quasicrystals, *Int. J. Mater. Res.*, 2013, **104**(4), p 380–385.
45. V. Stetsovych, F. Pagliuca, F. Dvorak, T. Duchon, M. Vorokhta, M. Aulicka, J. Lachnitt, S. Schernich, I. Matolinova, K. Veltruska, T. Skala, D. Mazur, J. Myslivecek, J. Libuda and V. Matolin, Epitaxial Cubic CeO Films via Ce-CeO Interfacial Reaction, *J. Phys. Chem. Lett.*, 2013, **4**(6), p 866–871.
46. D.L. Ye and J.H. Hu, *Utility Inorganic Materials Thermodynamics Data Handbook*, 2nd ed. Metallurgy Industry Press, Beijing, 2002, p 115
47. P. Wang, J. Li, C.Z. Lin, L. Yang, L. Peng, Y. Wang, C. Xiao and J.C. Chen, First-Principles Calculations of Electronic Structure and Mechanical Properties of Ti-Ni Intermetallic Compounds, *Trans. Nonferrous Met. Soc. China*, 2016, **26**(12), p 2546–2554.
48. C.G. Mccracken, Review of titanium. Powder-production methods, *Int. J. Powder Metall.*, 2010, **46**(5), p 19–26.
49. F.L. Hu, J. Li, Y.F. Tao and Y.H. Lv, Corrosion Behaviors of TiNi/Ti₂Ni Matrix Coatings in the Environment Rich in Cl Ions, *Surf. Coat. Technol.*, 2017, **311**, p 295–306.
50. Y.S. Tian, Growth Mechanism of the Tubular TiB Crystals In Situ Formed in the Coatings Laser-Borided on Ti-6Al-4V Alloy, *Mater. Lett.*, 2010, **64**(22), p 2483–2486.
51. X.M. Sui, J. Lu, X. Zhang, L. Sun and W.P. Zhang, Microstructure and Properties of TiC-Reinforced Ti₂Ni/Ti₅Si₃ Eutectic-Based Laser Cladding Composite Coating, *J. Therm. Spray Technol.*, 2020, **29**, p 1838–1846.
52. X.Q. Cai, D.P. Wang, Y. Wang and Z.W. Yang, Microstructural Evolution and Mechanical Properties of TiB₂-TiC-SiC Ceramics Joint Brazed Using Ti-Ni Composite Foils, *J. Eur. Ceram. Soc.*, 2020, **40**(9), p 3380–3390.
53. C.K. Sahoo and M. Masanta, Effect of Pulse Laser Parameters on TiC Reinforced AISI 304 Stainless Steel Composite Coating by Laser Surface Engineering Process, *Opt. Lasers Eng.*, 2015, **67**, p 36–48.
54. M.M. Quazi, M.A. Fazal, A.S.M.A. Haseeb, F. Yusof, H.H. Masjuki and A. Arslan, Effect of Rare Earth Elements and Their Oxides on Tribo-Mechanical Performance of Laser Claddings: A Review, *J. Rare Earths*, 2016, **34**(6), p 549–564.
55. Y.H. Qu, J.D. Xing, X.H. Zhi, J.Y. Peng and H.G. Fu, Effect of Cerium on the As-Cast Microstructure of a Hypereutectic High Chromium Cast Iron, *Mater. Lett.*, 2008, **62**(17–18), p 3024–3027.
56. B.B. Wu, N. Ni, X.H. Fan, X.F. Zhao, P. Xiao and F.W. Guo, Strength Degradation of SiC Fibers with a Porous ZrB₂-SiC Coating: Role of the Coating Porous Structure, *J. Eur. Ceram. Soc.*, 2020, **40**(4), p 961–971.
57. A.F.A. Hoadley and M. Rappaz, A Thermal Model of Laser Cladding by Powder Injection, *Metall. Trans. B*, 1992, **23B**(5), p 631–642.
58. J.W. Rutter and B. Chalmers, A Prismatic Substructure Formed During Solidification of Metals, *Can. J. Phys.*, 1953, **31**(1), p 15–39.
59. T.B. Massalaki, *Binary Alloy Phase Diagrams*, American Society for Metals, Metals Park, 1986, p 1
60. T. Ahmed and H.J. Rack, Phase Transformations During Cooling in α+β Titanium Alloys, *Mater. Sci. Eng. A Struct. Mater. Prop. Microstruct. Process.*, 1998, **243**(1), p 206–211.
61. J.J. Yang, H.C. Yu, J. Yin, M. Gao, Z.M. Wang and X.Y. Zeng, Formation and Control of Martensite in Ti-6Al-4V Alloy Produced by Selective Laser Melting, *Mater. Des.*, 2016, **108**, p 308–318.
62. J.L. Liu, H.J. Yu, C.Z. Chen, F. Weng and J.J. Dai, Research and Development Status of Laser Cladding on Magnesium Alloys: A REVIEW, *Opt. Lasers Eng.*, 2017, **93**, p 195–210.
63. R.D. Zhu, Z.Y. Li, X.X. Li and Q. Sun, Microstructure and Properties of the Low-Power-Laser Clad Coatings on Magnesium Alloy with Different Amount of Rare Earth Addition, *Appl. Surf. Sci.*, 2015, **353**, p 405–413.
64. F. Behzad, S.F. Wayne, L. Gladius and A. Ebrahim, A Review on Melt-Pool Characteristics in Laser Welding of Metals, *Adv. Mater. Sci. Eng.*, 2018, **11**, p 1–18.
65. P.A. Korzhavyi, L.V. Pourovskii, H.W. Hugosson, A.V. Ruban and B. Johansson, Ab Initio Study of Phase Equilibria in TiC_x, *Phys. Rev. Lett.*, 2002, **88**(1), p 015505.
66. N. Zarrinfar, P.H. Shipway, A.R. Kennedy and A. Saidi, Carbide Stoichiometry in TiC_x and Cu-TiC_x Produced by Self-propagating High-Temperature Synthesis, *Scr. Mater.*, 2002, **46**(2), p 121–126.
67. Y.X. Li, J.D. Hu, H.Y. Wang, Z.X. Guo and A.N. Chumakov, Thermodynamic and Lattice Parameter Calculation of TiC_x Produced from Al-Ti-C Powders by Laser Igniting Self-propagating High-Temperature Synthesis, *Mater. Sci. Eng. A STRUCT. Mater. Prop. Microstruct. Process.*, 2007, **458**(1–2), p 235–239.
68. Y.J. Yang, Z.H. Zheng, X. Wang, X.H. Liu, J.G. Man and J.S. Yoon, Microstructure and Tribology of TiB₂ and TiB₂/TiN Double-Layer Coatings, *Surf. Coat. Technol.*, 1996, **84**(1–3), p 404–408.
69. V. Geanta, I. Voiculescu and S. Tudoran, Effects of Fe and Mn on Microstructure and Microhardness of Titanium Alloys, *Rev. Chim.*, 2020, **71**(4), p 87–94.
70. H.C. Man, S. Zhang, F.T. Cheng and T.M. Yue, Microstructure and Formation Mechanism of In Situ Synthesized TiC/Ti Surface MMC on Ti-6Al-4V by Laser Cladding, *Scr. Mater.*, 2001, **44**(12), p 2801–2807.
71. B.L. Bramfitt, The Effect of Carbide and Nitride Additions on the Heterogeneous Nucleation Behavior of Liquid Iron, *Metall. Trans.*, 1970, **1**(7), p 1987–1995.
72. N. Hirosaki, S. Ogata and C. Kocer, Ab Initio Calculation of the Crystal Structure of the Lanthanide Ln₂O₃ Sesquioxides, *J. Alloys. Compd.*, 2003, **351**, p 31–34.
73. S. Shimada and J. Watanabe, Kodaira, Flux Growth and Characterization of TiC Crystals, *J. Mater. Sci.*, 1989, **24**(7), p 2513–2515.
74. S. Lartigue-Korinek, M. Walls, N. Haneche, L. Cha, L. Mazerolles and F. Bonnet, Interfaces and Defects in a Successfully Hot-Rolled Steel-Based Composite Fe-TiB₂, *Acta Mater.*, 2015, **98**, p 297–305.

75. H.H. Xiong, H.N. Zhang and J.H. Dong, Adhesion Strength and Stability of TiB₂/TiC Interface in Composite Coatings by First Principles Calculation, *Comput. Mater. Sci.*, 2017, **127**, p 244–250.
76. O. Dumas, L. Malet, B. Hary, F. Prima and S. Godet, Crystallography and Reorientation Mechanism Upon Deformation in the Martensite of an α - α' Ti-6Al-4V Dual-Phase Microstructure Exhibiting High Work-Hardening Rate, *Acta Mater.*, 2021, **205**, p 116530.
77. C. Leyens and M. Peters, *Titanium and Titanium Alloys: Fundamentals and Applications*, Wiley, Hoboken, 2003.
78. J.F. Archard, Contact and Rubbing of Flat Surfaces, *J. Appl. Phys.*, 1953, **24**(8), p 981–988.
79. M.N. Gardos, Magnéli Phases of Anion-Deficient Rutile as Lubricious Oxides. Part II. Tribological Behavior of Cu-Doped Polycrystalline Rutile (TiO_{2n-1}), *Tribol. Lett.*, 2000, **8**(2–3), p 79–96.

Publisher's Note Springer Nature remains neutral with regard to jurisdictional claims in published maps and institutional affiliations.